Early fluid activity on Ryugu inferred by oxygen, carbon, and [53]Mn-[53]Cr isotopic analyses of carbonates and magnetite

Kaitlyn A. McCain[1,18*], Nozomi Matsuda[1*], Ming-Chang Liu[1,19], Kevin D. McKeegan[1], Akira

Yamaguchi[2], Makoto Kimura[2], Naotaka Tomioka[3], Motoo Ito[3], Naoya Imae[2], Masayuki Uesugi[4],

Naoki Shirai[5,6], Takuji Ohigashi[7,8], Richard C. Greenwood[9], Kentaro Uesugi[4], Aiko Nakato[10],

Kasumi Yogata[10], Hayato Yuzawa[7], Yu Kodama[11,17], Kaori Hirahara[12], Ikuya Sakurai[13], Ikuo

Okada[13], Yuzuru Karouji[10], Satoru Nakazawa[10], Tatsuaki Okada[10], Takanao Saiki[10], Satoshi

Tanaka[10], Fuyuto Terui[14], Makoto Yoshikawa[10], Akiko Miyazaki[10], Masahiro Nishimura[10], Toru

Yada[10], Masanao Abe[10], Tomohiro Usui[10], Sei-ichiro Watanabe[15], and Yuichi Tsuda[10,16].

Affiliations

[1]Department of Earth, Planetary, and Space Sciences, UCLA, Los Angeles, CA 90095, USA

[2]National Institute of Polar Research (NIPR), Tachikawa, Tokyo 190-8518, Japan

[3]Kochi Institute for Core Sample Research, X-star, Japan Agency for Marine-Earth Science

Technology (JAMSTEC), Nankoku, Kochi 783-8502, Japan

[4]Japan Synchrotron Radiation Institute (JASRI/SPring-8), Sayo, Hyogo 679-5198, Japan

[5]Graduate School of Science, Department of Chemistry, Tokyo Metropolitan University, Hachioji,

Tokyo 190-0397, Japan

[6]Department of Chemistry, Faculty of Science, Kanagawa University, Hiratsuka, Kanagawa 259-

1293, Japan

[7]UVSOR Synchrotron Facility, Institute for Molecular Science, Okazaki, Aichi 444-8585, Japan,

[8]Institute of Materials Structure Science, High Energy Accelerator Research Organization,

Tsukuba, Ibaraki 305-0801, Japan

[9]Planetary and Space Sciences, The Open University, Milton Keynes MK7 6AA, UK

26 [10]Institute of Space and Astronautical Science (ISAS), Japan Aerospace Exploration Agency

27 (JAXA), Sagamihara, Kanagawa 252-5210, Japan,

28 [11]Marine Works Japan, Ltd., Yokosuka, Kanagawa 237-0063, Japan

29 [12]Department of Mechanical Engineering, Osaka University, Suita, Osaka 565-0871, Japan

30 [13]Synchrotron Radiation Research Center, Nagoya University, Nagoya, Aichi 464-8603, Japan

31 [14]Kanagawa Institute of Technology, Atsugi, Kanagawa 243-0292, Japan

32 [15]Graduate School of Environmental Studies, Nagoya University, Nagoya, Aichi 464-8601, Japan

33 [16]The Graduate University for Advanced Studies (SOKENDAI), Hayama, Kanagawa 240-0193,

34 Japan

35 [17]Now at Toyo Corp.

36 [18]Now at Jacobs JetsII Contract, NASA Johnson Space Center, Mail Code XI3, Houston, TX,

37 77058, USA

38 [19]Now at Lawrence Livermore National Laboratory, Livermore, CA, 94550, USA

39

40 Kaitlyn A. McCain and Nozomi Matsuda contributed equally

41 [*]Corresponding author (kamccain@ucla.edu and nozomi32@ucla.edu)

42

43

44   **Abstract**

45   Samples from asteroid Ryugu returned by the Hayabusa2 mission contain evidence of extensive

46   alteration by aqueous fluids and appear related to the CI chondrites. To understand the sources of

47   the fluid and the timing of chemical reactions occurring during the alteration processes, we

48   investigated the oxygen, carbon, and ^{53}Mn-^{53}Cr systematics of carbonate and magnetite in two

49   Ryugu particles. We find that the fluid was initially between 0−20 °C and enriched in ^{13}C, and ^{17}O

50   and ^{18}O, and subsequently evolved towards lighter carbon and oxygen isotopic compositions as

51   alteration proceeded. Carbonate ages show that this fluid-rock interaction took place within the

52   first ~1.8 million years of solar system history, requiring early accretion either in a planetesimal

53   less than ~20 km in diameter or within a larger body which was disrupted and reassembled.

54

55

56   **Main text**

57   The Hayabusa2 mission returned approximately 5.4 g of material from the C-type asteroid

58   Ryugu. This material is highly aqueously altered and resembles the rare CI (Ivuna-type) chondrite

59   meteorites, with abundant Mg-phyllosilicate, pyrrhotite, magnetite, and carbonate signifying

60   extensive fluid evolution on Ryugu's parent body[1–5]. Because aqueous alteration products such as

61   magnetite and carbonate record information about the fluid from which they form, isotopic

62   measurements of these components can be used to constrain the timing and characteristics of

63   aqueous alteration of Ryugu materials.

64   In addition to their mineralogical similarities, the bulk oxygen isotopic compositions of the

65   Ryugu particles and CI chondrites are also similar[3–6]. These values are primarily defined by the

66   phyllosilicate matrix, the most abundant component in both Ryugu and the CI chondrites, with

67   ~64–88 vol%[3] and ~83–94 vol%[7,8], respectively. Oxygen isotopic compositions of CI components

68   such as carbonate, anhydrous silicate, phyllosilicate, and magnetite have been used to estimate the

69   temperatures of final equilibration between carbonate and phyllosilicate to ~50–150 °C[9,10], and

70   radiometric dating of secondary minerals has constrained the timing of fluid alteration to ~4–6

71   Myr after Ca, Al-rich inclusions (CAI) formation[11,12]. However, the CI chondrites have been

72   exposed to various degrees of terrestrial alteration, which appear to have affected the bulk oxygen

73   isotopic compositions[6]. Ryugu particles therefore represent a unique opportunity to study pristine

74   samples of hydrated asteroidal material.

75   Of the various alteration products found in hydrated extraterrestrial materials like returned

76   Ryugu particles and CI chondrites, carbonate minerals are of particular interest because they can

77   be dated using the short-lived ^{53}Mn-^{53}Cr chronometer ($t_{1/2} = 3.7$ Myr), thereby tracking when liquid

78   water was present and establishing a timescale for the accretion and alteration of carbonaceous

79   planetesimals. Stable isotope studies of the major elements O and C can also provide insight into

80   the sources of the fluids present as well as the temperatures and reactions occurring in the asteroid

81   or its progenitor. To preserve the petrologic context and minimize consumption of precious Ryugu

82   material, these analyses can be performed in-situ with high spatial resolution using Secondary Ion

83   Mass Spectrometry (SIMS) to sputter material from individual mineral grains with a spot size of

84   ~3–15 µm (see Methods). This technique has also been applied to analyses of carbonate and other

85   secondary minerals in CM and CI carbonaceous chondrites, which facilitates comparison between

86   the returned Ryugu particles and previously studied meteorite samples.

87   The oxygen isotopic systematics of aqueous alteration products in carbonaceous chondrite

88   meteorites have been extensively studied[10,13–25] and used to infer the extent of equilibration

89   between co-accreted water ice, inferred to be ^{17,18}O-enriched[26] with positive $\Delta^{17}O$ ($\Delta^{17}O = \delta^{17}O -$

90    $0.52 \times \delta^{18}O$), and anhydrous silicates[9,24,27] with negative $\Delta^{17}O$ on the parent body, thereby tracking

91   the sequence of alteration. In addition, if two secondary phases with the same $\Delta^{17}O$ are identified,

92   the difference in $\delta^{18}O$ between the two phases can be used to calculate an equilibrium formation

93   temperature, based on the assumption that they precipitated from the same water

94   composition[9,13,14,23]. Previously, CI chondrite formation temperatures have been estimated based

95   upon the phyllosilicate-carbonate pair[9,10].   The oxygen isotopic compositions of magnetite, if

96   found to be in equilibrium with other secondary phases, can be used in a similar fashion[23].

97   The carbon isotopic compositions of carbonate have been used to infer the contributions of

98   various C sources, such as insoluble and soluble organic matter[28,29] and isotopically heavy CO_2–

99   CO ices[30,31], to the fluids in the carbonaceous chondrite parent bodies. In principle, carbon isotope

100   compositions can also track reactions occurring within the fluid such as methane formation and

101   loss[19,22,23,32], oxidation of organic material[18,20], and CH_4–CO equilibration[23,33]. However, such

102   studies have thus far been limited to carbonate from the CM (Mighei-type), Tagish Lake (C2-

103   ungrouped)[34], and Flensburg (C1-ungrouped)[25] chondrites; few in-situ C isotopic measurements

104   have been conducted on CI carbonate[35].

105   The timing and duration of carbonate formation can be constrained in favorable

106   circumstances by using Mn-Cr dating, and these ages can also be used to constrain the accretion

107   time of the parent bodies from which samples originate. Carbonate minerals are an ideal target for

108   this analysis as they strongly fractionate Mn from Cr during their formation, leading to large

109   excesses in radiogenic ^{53}Cr through which a ^{53}Mn/^{55}Mn ratio at the time of carbonate formation

110   can be inferred. Previous in-situ studies of highly-altered carbonaceous chondrites have found that

111   most carbonate grains in these meteorite classes formed between 4–6 Myr after CAIs, leading to

112   inferences, based upon models of planetesimal thermal evolution, that carbonate formation

113   occurred in large (> 50km radius) parent bodies which accreted 3–4 Myr after CAI

114   formation[11,12,36]. However, deriving initial ^{53}Mn/^{55}Mn ratios of carbonate based on in-situ SIMS

115   analyses requires standards that closely match the chemical composition of the target mineral to

116   determine the Mn/Cr ratio accurately (i.e., are 'matrix-matched'), particularly with regard to the

117   Fe content of the carbonate[37–39]. Previous studies which targeted dolomite were performed using

118   non-matrix-matched standards (primarily calcite) for the Mn/Cr ratio, which can affect the

119   accuracy of the results[38,39]. In this work, we use matrix-matched calcite, dolomite, and magnesite

120   standards to obtain the ^{55}Mn/^{52}Cr ratios of respective mineral phases in Ryugu.

121   Ryugu particles A0037 and C0009, which were acquired from the 1st and 2nd touchdown

122   sites respectively[3], are dominated by minerals produced via aqueous alteration[1,3]. A0037 contains

123   a much higher abundance of carbonate (21.2 vol%) than does C0009 (1.8 vol%)[3]. Carbonates

124   found in these two particles are primarily dolomite ($CaMg(CO_3)_2$, Figure 1a; see also Figure 2 in

125   Yamaguchi et al., 2022) with minor occurrence of Ca-carbonate ($CaCO_3$, Figure 1b and c; see also

126   Supplementary Figure 6 in Yamaguchi et al., 2022) and breunnerite ($(Mg,Fe,Mn)CO_3$, see

127   Supplementary Figure 6 in Yamaguchi et al., 2022) in C0009. Both particles contain magnetite

128   (3.6 vol%)[3] with a variety of morphologies, often enclosed within dolomite (Figure 1a, see also

129   Supplementary Figure 6 in Yamaguchi et al., 2022). Detailed petrological and mineralogical

130   descriptions of both particles are reported by previous studies[3] and Yamaguchi et al. (2022).

131

132   RESULTS

133   *Oxygen isotopic composition of carbonate and magnetite*

134   The oxygen isotopic compositions of dolomite and magnetite in particles A0037 and

135   C0009 and Ca-carbonate in C0009 are shown in Figure 2 and listed in Supplementary Tables 1–2.

136   The oxygen isotopic compositions of dolomites mostly plot near the terrestrial mass fractionation

137   (TF) line, however several dolomite grains have positive $\Delta^{17}O$ well resolved from 0‰, up to a

138   maximum of +1.6 ± 0.3‰ (2σ) for a dolomite grain found in A0037 and +1.4 ± 0.9‰ (2σ) for a

139   dolomite grain found in C0009. The $\delta^{18}O$ values of dolomite grains are also somewhat variable,

140   ranging from +25‰ to +34‰ in A0037 and from +22‰ to 27‰ in C0009. The range of oxygen

141   isotopic compositions of Ryugu dolomite in A0037 and C0009 is in good agreement with prior in-

142   situ analyses of CI-chondrite dolomite[24] and Ryugu dolomite from other particles[4,5] (see Figure 2).

143   Ryugu dolomite is distinct from dolomite found in Flensburg (C1-ungrouped), for which $\Delta^{17}O$

144   ranges from −4.1 to −2.4 ‰[25]. The $\Delta^{17}O$ values of magnetite show a limited range from +2.1‰ to

145   +3.9‰ for A0037 and from +1.7‰ to +3.9‰ for C0009, which nevertheless exceeds analytical

146   uncertainty (MSWD = 5.2 (A0037) and 3.5 (C0009)). The $\delta^{18}O$ values of magnetite range from

147   −11‰ to +3‰. The $\delta^{18}O$ and $\Delta^{17}O$ values of magnetite in A0037 and C0009 are similar to those

148   observed in bulk analyses of CI chondrite magnetite[14] and magnetite in some other Ryugu

149   particles[5], but differ from other Ryugu particles containing magnetite with lower $\Delta^{17}O$ values[4] (see

150   Figure 2). The Ca-carbonate found in particle C0009 ranges in composition from $\Delta^{17}O$ ~0 to

151   +2.2‰ and $\delta^{18}O$ ~+34‰ to +39‰, which differs significantly from calcite separated from Orgueil

152   ($\Delta^{17}O$ ~0‰ and $\delta^{18}O$ = +25.5‰)[24] and from Flensburg calcite ($\Delta^{17}O$ ~ −3.8 to −1.1 ‰ and $\delta^{18}O$

153   +13.5 to +32.4 ‰)[25].

Carbon isotopic compositions of carbonate

155   Dolomite in both Ryugu particles shows a wide range of $\delta^{13}C$ values from 55.4‰ to 74.5‰

156   (Figure 3 and Supplementary Table 3). Dolomite in A0037 appears to follow a bimodal distribution

157   with $\delta^{13}C$ peaks at ~55 and ~70‰. Dolomite (and some Ca-carbonate) in C0009 show $\delta^{13}C$ ranging

158   from 64‰ to 75‰, with one Ca-carbonate enriched in $\delta^{13}C$ at 97‰ (Figure 3 and Supplementary

159   Table 3). These $\delta^{13}C$ values are consistent with bulk measurements of Orgueil carbonates[33] and

160   are similar to the compositions of carbonates in Tagish Lake[34], but are more enriched in ^{13}C than

161   calcite and dolomite in Flensburg[25].

Mn-Cr dating of carbonate

163   We measured $^{55}Mn/^{52}Cr$ and $^{53}Cr/^{52}Cr$ ratios for 20 spots on dolomite in A0037 and 16

164   spots on dolomite, breunnerite, and Ca-carbonate in C0009 (Supplementary Table 4) and corrected

165   for the relative sensitivity between Mn and Cr using matrix-matched, ^{52}Cr-implanted terrestrial

166   carbonate standards[39]. The analysis conditions, standards development, and Mn-Cr data on Ryugu

167   carbonates are detailed in the Methods and Supplementary text. The data show ^{53}Cr excesses that

168   are well-correlated with $^{55}Mn/^{52}Cr$ (Figure 4) implying initial $^{53}Mn/^{55}Mn$ of $(6.8 \pm 0.5) \times 10^{-6}$

169   (MSWD = 0.7) for A0037 dolomite and $(6.1 \pm 0.9) \times 10^{-6}$ (MSWD = 0.3) for C0009 (all errors

170   2SE). By calibrating these initial ratios relative to the initial $^{53}Mn/^{55}Mn$ ratio[40] of the D'Orbigny

171 angrite, which has a well-defined absolute crystallization age[41,42], we calculate that A0037 and

172 C0009 carbonates formed at 4566.9 ± 0.4 Ma and 4566.3 ± 0.8 Ma, respectively. Assuming 'time-

173 zero' defined by a $^{207}Pb/^{206}Pb$ closure age[43] for CAIs of 4567.3 Ma, the carbonates in Ryugu

174 formed within the first 1.8 Myr of solar system origin—earlier than inferred from previous studies

175 of carbonaceous chondrites[11,12,25,36,44] and other Ryugu particles[4,5].

176

177 DISCUSSION

178   A Ca-carbonate grain designated 'Ca 2' has $\Delta^{17}O$ = +2.2‰, the highest value of $\Delta^{17}O$ we

179 have measured in Ryugu carbonate, which suggests that it recorded an early phase of fluid

180 evolution when a relatively ^{17}O- and ^{18}O-enriched fluid[26] was less equilibrated with ^{16}O-rich

181 nebular solids[27]. As previously described[45], the Ca-carbonate 'Ca 2' is isolated in the matrix and

182 surrounded by an iron sulfide rim (Figure 1b), while other Ca-carbonates are found as chains and

183 clusters of individual grains with no rims (Figure 1c), further supporting that the formation

184 conditions which produced Ca 2 were distinct from those that produced other Ca-carbonates[45]. We

185 note that the petrology of 'Ca 2' closely resembles 'Type 1' calcites identified in the CM

186 chondrites[20], which have been interpreted to be have formed in early stages of fluid alteration as

187 pores produced by melting water ice were cemented by carbonate precipitation[17]. Figure 3 shows

188 that 'Ca 2' is also enriched in ^{13}C at $\delta^{13}C$ = +97‰, suggesting that carbon in the fluid was initially

189 isotopically heavy and derived from outer solar system CO_2 ices, similar to what has been inferred

190 for some carbonaceous chondrites[30,31,34]. Therefore, we conclude that Ryugu accreted in the outer

191 solar system beyond the CO_2 ice line, consistent with previous observations of bulk H and N

192 isotopes in Ryugu particles that suggest an outer solar system origin[3].

193   The population of Ca-carbonate in particle C0009 shows a range in $\Delta^{17}O$ of ~0 to +2.2‰,

194   following a mass-independent trend which requires that the O isotopic composition of the fluid

195   evolved over the course of Ca-carbonate precipitation. This is in contrast to calcite grains found in

196   Orgueil[24], which follow a mass-dependent trend, i.e. constant $\Delta^{17}O$, with a restricted range in $\delta^{18}O$.

197   We suggest that this distinction reflects a difference in the extent of alteration processes

198   experienced by Ryugu and by Orgueil: the Ca-carbonate in Ryugu recorded the progress of

199   equilibration between fluid and ^{16}O-rich anhydrous silicate[27], whereas calcite in Orgueil

200   precipitated after this equilibration had been established.

201   Magnetite in both particles and the "Ca 2" Ca-carbonate grain (Figure 1a and b; see also

202   Supplementary Figure 6f in Yamaguchi et al., 2022) in C0009 share the same $\Delta^{17}O$ values (within

203   uncertainty) that is higher than the $\Delta^{17}O$ of dolomite and other Ca-carbonates, reflecting a less-

204   equilibrated fluid composition. We conclude that magnetite and Ca-carbonate like 'Ca 2' were

205   among the earliest minerals to precipitate during the alteration of the Ryugu protolith, predating

206   most carbonate formation. If the 'Ca 2' Ca-carbonate and magnetite formed in equilibrium with

207   the same fluid[45], we estimate the formation temperature at this early stage of alteration using

208   equilibrium thermometry of calcite and magnetite[46] to be 0−20 °C. Further discussion of

209   magnetite-H_2O and calcite-H_2O oxygen isotopic fractionation can be found in the Supplementary

210   text.

211   Dolomite in this study and bulk Ryugu particles share the same value of $\Delta^{17}O$ within our

212   uncertainties[6]. The bulk oxygen isotopic composition is dominated by phyllosilicates, with

213   variable contributions from carbonates which can increase the $\delta^{18}O$ of the bulk analysis. If we

214   suppose that the weighted average of bulk Ryugu $\delta^{18}O$ from Greenwood et al. (2022) of 15.88 ±

215   4.85‰ (2SD) represents the composition of phyllosilicate, we can calculate an equilibrium

216   formation temperature using this phyllosilicate-dominated bulk analysis and our observed range

217   of dolomite $\delta^{18}O$ values (+25–34‰). Using experimentally-determined fractionation factors for

218   dolomite[47] and brucite[48], we constrain the equilibration temperature of dolomite and phyllosilicate

219   to 88–240 °C. Further discussion of phyllosilicate-H_2O and dolomite-H_2O fractionation can be

220   found in the Supplementary text.

221   We suggest the following order for the sequence of aqueous alteration on Ryugu: first,

222   magnetite and Ca-carbonates like 'Ca 2' precipitated from aqueous fluids with high $\Delta^{17}O$ at T <20

223   °C with the carbon isotopic composition of the fluid dominated by that of CO_2 ice. As the fluid

224   continued to exchange oxygen with ^{16}O-rich anhydrous silicates[27], additional Ca-carbonate

225   precipitated as $\Delta^{17}O$ fell from ~+1.1 to 0 ‰. Finally, most dolomite formed at about $\Delta^{17}O = +0.4$

226   ‰ after Mg had been added to the fluid by alteration of Mg-rich silicates to form phyllosilicates

227   with similar $\Delta^{17}O$ to dolomite. The relatively homogeneous $\Delta^{17}O$ composition of dolomite

228   indicates that the pace of evolution of the fluid's oxygen isotopic composition had slowed by the

229   time of dolomite formation. Petrographic observations of magnetite inclusions enclosed in

230   dolomite but not in Ca-carbonate support this sequence of events (Figure 1; see also Figure 2c in

231   Yamaguchi et al., 2022) [45].

232   Carbon and oxygen isotopic analyses performed on the same grains were used to explore

233   correlations between the two isotopic systems. Figure 5 illustrates that $\delta^{13}C$ is correlated with $\delta^{18}O$

234   (upper panel) and $\Delta^{17}O$ (lower panel), similar to trends observed for some CM chondrites[33]. This

235   observation suggests that methane formation via serpentinization of the protolith followed by loss

236   to space did not strongly affect the $\delta^{13}C$ of Ryugu carbonate, as methane release would enrich ^{13}C

237   in the fluid over time[20,32]. In contrast, we observe that carbonate formed from less-equilibrated

238   water (e.g., with higher $\delta^{18}O$ and $\Delta^{17}O$) is also the most ^{13}C-enriched. One possible scenario could

239   be that the initial unequilibrated fluid composition, presumably similar to the fluid recorded by

240   'Ca 2', evolved towards lower $\delta^{13}C$ as the fluid interacted with and oxidized Ryugu's relatively

241   ^{13}C-depleted organic matter[3].

242   The old ages measured in Ryugu carbonate stand in contrast to ages obtained from

243   carbonate in carbonaceous chondrites, most of which were thought to have formed 4–6 Myr after

244   CAIs,[11,12,36,44]. Ryugu carbonate in C0009 and A0037 is also slightly older than carbonate found

245   in Flensburg[25]. This difference arises from our use of matrix-matched standards, as opposed to

246   calcite standards used exclusively in previous studies, to determine the Mn/Cr of the carbonates.

247   Had we corrected measured Mn^+/Cr^+ using a relative sensitivity factor derived only from analyses

248   of calcite, we would have obtained ages of 3.0 Myr and 3.5 Myr after CAI formation for A0037

249   and C0009 carbonate respectively, approaching the range of ages previously determined for

250   carbonates in carbonaceous chondrites[11,12,36,44].

251   These old carbonate formation ages suggest a significantly different formation scenario for

252   Ryugu than those previously proposed for the asteroid parent bodies of carbonaceous chondrites.

253   Our data show that aqueous fluids responsible for carbonate formation were active on Ryugu (or

254   its progenitor asteroid) early in Solar System history, within the first ~1.8 Myr after CAI formation.

255   At that time, ^{26}Al in chondritic material was still at the level of $^{26}Al/^{27}Al$ ~10^{-5}, abundant enough

256   to melt accreted ices and drive aqueous alteration. However, for ^{26}Al heating to not be so intensive

257   as to cause water loss or even silicate melting and chemical differentiation, Ryugu must have

258   initially accreted as a small asteroid which could effectively conduct heat away from its interior to

259   cool itself by radiation. The inferred presence of co-accreted CO_2 ice constrains the initial

260   temperature of the parent body to below the sublimation temperature of CO_2. By modeling parent

261   bodies accreting as mixtures of 50% chondritic material and 50% water ice[10,49] at an initial

262   temperature of 78 K, we find that parent bodies accreting before 1.8 Myr must be smaller than 20

263   km in diameter for the internal temperature to remain below 400 K[50,51]. In such bodies, the interior

264   4 km reaches the melting point of water within 0.4 Myr after accretion, and remains warm enough

265   to support liquid water for an additional 1.1 to 1.5 Myr.

266   Alternatively, it could be possible to form Ryugu components in a progenitor body larger

267   than 20 km in diameter which was later disrupted by impact before reaching peak temperatures.

268   Ryugu is a ~1 km diameter asteroid inferred, like many asteroids, to be a 'rubble pile' characterized

269   by large internal void spaces and a low bulk density $(1{,}190 \pm 20 \text{ kg m}^{-3})$[52]. A multi-stage scenario

270   of brecciation and reassembly is also supported by petrographic and shock characteristics observed

271   in Ryugu particles[3,45,53]. This view is very different from prior estimates of parent body size and

272   accretion times based upon younger carbonate ages, which suggested that CM and CI parent bodies

273   were >50 km in diameter and accreted ~3–3.5 Myr after CAI formation[11,12,36].

274   An early formation scenario for C-type asteroids has implications for models seeking to

275   understand the origins of the so-called 'isotopic dichotomy' within the solar nebula. In this

276   framework, the early solar system was divided into two reservoirs, one characterized by isotopic

277   compositions similar to those of the volatile-rich carbonaceous chondrites (CC), and the other

278   being isotopically similar to the compositions of volatile-depleted ordinary-chondrite, enstatite-

279   chondrite, and terrestrial materials[54] (collectively known as the non-carbonaceous (NC) isotopic

280   reservoir). Whereas the NC group accreted from materials formed in the inner solar system, the

281   CC group is thought to have accreted in the outer solar system, beyond the snow line. Based on

282   ^{182}Hf-^{182}W ages of iron meteorites with CC affinities, it has been suggested that some

283   planetesimals in the outer solar system accreted within ~1 Myr of CAI formation[55]. This timescale

284   is consistent with such objects having melted and chemically differentiated into core-mantle

285   structures due to ^{26}Al heating, and is also consistent with the accretion time of NWA 011, a basaltic

286   achondrite with CC affinities that accreted within 1.6 Myr of CAI formation[56]. Based on previous

287   Mn-Cr dating of carbonates it was thought that CM and CI chondrites escaped such heating by

288   virtue of having accreted at later times, after most ^{26}Al had decayed. However, early formation

289   for undifferentiated CC material, such as that from Ryugu, requires an explanation (e.g., formation

290   in a small body or early disruption by impact) for the simultaneous existence of differentiated and

291   unmelted CC materials. Similarly, models of accretion and transport in the disk which invoke a

292   late formation time for carbonaceous chondrite parent bodies[57] should consider the implications of

293   early formation of these objects.

Methods

Petrographic characterization

The detailed scanning electron microscope (SEM) and electron probe microanalysis (EPMA) methods are reported by Yamaguchi et al. (2022)[45]. Laser micro-Raman spectroscopy[45] was used to attempt to distinguish whether Ca-carbonate in the Ryugu C0009 was calcite or aragonite, but not enough of the band peak was measured to distinguish between the $CaCO_3$ polymorphs.

Secondary ion mass spectrometry

In-situ oxygen, carbon, and Mn-Cr isotopes analyses of Ryugu carbonates and magnetite were performed using the UCLA CAMECA ims-1290 ion microprobe. The Ryugu A0037 and C0009 particles were mounted in epoxy and polished under dry conditions and coated with a thin layer of Au for SIMS analyses after petrographic characterization. After SIMS analysis, all pits were observed by SEM (Tescan Vega) at UCLA. Analyses found to overlap inclusions, cracks, or voids were discarded. In all stable isotope analyses, calcite, magnetite, and a suite of 4 dolomite standards of various Fe compositions were measured to quantify the instrumental mass fractionation (IMF) as a function of Fe content[58,59]. The chemical and isotopic compositions of these reference materials are listed in Supplementary Table 5.

Oxygen isotope analysis

Oxygen isotope analyses were performed with a focused Cs^+ primary ion beam with 20 kV total accelerating voltage. Based on the size of the grains analyzed, we used three different primary beam conditions: 3O-I (~3 nA) with ~15 µm spot for dolomite, 3O-II (~700 pA) with ~10 µm spot for dolomite, and 3O-III (~60 pA) with ~ 3µm spot for dolomite, Ca-carbonate, and magnetite. A

318 normal incidence electron gun was used for charge compensation. The oxygen isotopic

319 compositions are reported as per mil deviations relative to standard mean ocean water (SMOW),

320 which can be calculated by using $\delta\,^{x}O = \left[\dfrac{(^{x}O/^{16}O)_{sample}}{(^{x}O/^{16}O)_{SMOW}} - 1 \right] \times 1000$, where x = 17 or 18. The

321 deviation from the terrestrial fractionation line is expressed as $\Delta^{17}O_{SMOW} = \delta^{17}O_{SMOW} - 0.52 \times$

322 $\delta^{18}O_{SMOW}$.

323   In session 3O-I, secondary $^{16}O^{-}$, $^{17}O^{-}$, and $^{18}O^{-}$ ions were collected simultaneously using

324 three Faraday cups (FCs) to achieve the highest possible precision. Typical $^{16}O^{-}$ current was

325 equivalent to ~3×10^{9} counts/sec for the MS1317J dolomite standard. The mass resolution power

326 (MRP) was set to ~5500 for $^{17}O^{-}$. In the second session (3O-II), the secondary ions were measured

327 simultaneously using two FCs (for $^{16}O^{-}$ and $^{18}O^{-}$) and the axial electron multiplier (EM; for $^{17}O^{-}$)

328 under the mass resolution of ~5800 for $^{17}O^{-}$ with a typical count rate for $^{16}O^{-}$ ~7.8×10^{8} cps (for

329 MS1317J standard). In the third session (3O-III), we used a FC (for $^{16}O^{-}$) and two EMs (for $^{17}O^{-}$

330 and $^{18}O^{-}$) in multicollection mode. The secondary ion count rates of $^{16}O^{-}$ were ~6.1×10^{7} cps, ~5.8

331 $\times 10^{7}$ cps, and ~6.4×10^{7} cps for MS1317J, calcite, and magnetite, respectively. The MRP was

332 ~5600. Ion intensities were corrected for background and yield (FC) or deadtime (EM) as

333 appropriate for each detector.

334   The contribution of $^{16}OH^{-}$ tail to the $^{17}O^{-}$ signal was determined by using the ratio of the

335 ion signal measured at the tail of the $^{16}OH^{-}$ peak on the high mass end (mass unit = 17.00274 +

336 0.00361) to that measured at the center of the $^{16}OH^{-}$ peak and assuming a symmetric peak. This

337 ratio was then multiplied by the $^{16}OH^{-}$ count rate on the unknown samples recorded at the end of

338 each spot analysis. All reported $\delta^{17}O$ values have been corrected for the $^{16}OH^{-}$ tail (Supplementary

339 Tables 1 and 2). The corrections for the $^{16}OH^{-}$ tail range from ~0.1 to 1.0 ‰.

340   The compositional dependence of instrumental bias (i.e., the "matrix effect" on

341   instrumental mass fractionation) was calibrated using an equation similar to that suggested in

342   Śliwiński et al. (2016)[58]. Error bars represent 2σ analytical uncertainty accounting for both the

343   internal measurement precision (standard error of mean over cycles measured) and the external

344   reproducibility (standard error of mean over standards measured) for bracketing measurements of

345   the standards; $\sigma^2 = (\text{SEM}_{unknown})^2 + (\text{SEM}_{standard})^2$.

346

347   *Carbon isotope analysis*

348   Carbon isotope analysis of carbonate was carried out using a focused Cs^+ ion primary beam

349   of ~600 to 700 pA. Secondary $^{12}C^-$ and $^{13}C^-$ ions were simultaneously detected using a FC and

350   EM, respectively. A normal incidence electron gun was used for charge compensation. The typical

351   count rate of $^{12}C^-$ was ~5.5–6 $\times10^6$ cps for MS1317J. The instrumental bias was corrected using

352   MS1317J with a $\delta^{13}C_{VPDB}$ value of $-1.20‰$ ($^{13}C/^{12}C = 0.011167$) and optical calcite with a

353    $\delta^{13}C_{VPDB}$ value of $1.42‰$ ($^{13}C/^{12}C = 0.011196$) for dolomite and Ca-carbonate, respectively.

354   We defined the bias as

355
$$(1)\ \text{bias} = \frac{\left(^{13}C/^{12}C\right)_m}{\left(^{13}C/^{12}C\right)_t}$$

356   where "m" and "t" stand for "measured" and "true" isotope ratios, respectively. Error bars

357   represent 2σ analytical uncertainty including both the internal measurement precision and the

358   external reproducibility for standard measurements.

359

360   *Mn-Cr isotope analysis*

361   Mn-Cr analyses of carbonates were carried out using a 1nA $^{16}O_3^-$ primary ion beam

362   generated by a Hyperion-II plasma ion source. For dolomite and magnesite with sufficient Mn

363   content, secondary $^{52}Cr^+$, $^{53}Cr^+$, and $^{55}Mn^+$ ions were collected simultaneously using two EMs (for

364     $^{52}Cr^+$ and $^{53}Cr^+$) and an FC (for $^{55}Mn^+$). A MRP of ~5500 was used to separate $^{52}Cr^+$ from $^{28}Si^{24}Mg^+$

365   and $^{53}Cr^+$ from $^{52}CrH^+$. For dolomite and calcite with low Mn concentrations, $^{55}Mn^+$ was collected

366   using an EM in peak-switching mode. Analysis spots were presputtered using an 8×8 or a 4×4

367   μm raster to remove surface Cr contamination before focusing the beam to a tighter raster (5×5

368   or 2×2 μm) for the analysis, resulting in an effective spot size of ~8×10 μm^2. The instrumental

369   mass fractionation for Cr was corrected by comparison to repeated measurements of the 1317J

370   dolomite, which contains trace amounts of terrestrial Cr ($^{53}Cr/^{52}Cr = 0.113459$)[60]. The relative

371   sensitivity factor between ^{55}Mn and ^{52}Cr is defined as

372 $$(2)\ RSF = \frac{(55Mn/52Cr)_{True}}{(55Mn/52Cr)_{SIMS}}$$

373   and was determined using a combination of San Carlos Olivine and ion-implanted carbonate

374   standards. Prior to the Mn-Cr analysis, the local distribution of ^{52}Cr was assessed using scanning

375   ion imaging to avoid regions with high ^{52}Cr background, which can indicate contamination from

376   Cr-rich phases.

377   Calculation of the isochron slope was performed using the 'fit_bivariate' python module,

378   an implementation of the York et al. (2004) line fitting algorithm[61].

379

Data availability

Correspondence and requests for materials should be addressed to K.A.M. and N.M. All analytical data related to this manuscript will be put on the JAXA Data ARchives and Transmission System (https://www.darts.isas.jaxa.jp/curation/hayabusa2) after a one-year proprietary period.

Author contributions

403   K.A.M. and N.M. led the project and wrote the initial draft. K.A.M., N.M., M-C.L., A.Y.,

404   N.T., M.I., M.U., N.I., N.S., T. Ohigashi, M.K., K.U., A.N., KY., H.Y., and Y.K. conducted

405   sample handling, preparation, and mounting processes of Ryugu grains. M.I., N.T., T. Ohigashi,

406   M.U., K.U., H.Y., Y.K., K.H., I.S., I.O., and K.U. developed universal sample holders for multiple

407   instruments. A.Y., M.K., N.I., M.I., and N.T. performed SEM-EDS analysis. A.Y. conducted

408   EPMA analysis and data reduction. K.A.M., N.M., and M.-C.L. carried out oxygen, carbon, and

409   Mn-Cr isotopes measurements of anhydrous carbonate and magnetite with SIMS. A.N., K.Y.,

410   A.M., M.N., T.Y., T. Okada., M.A., and T.U lead the JAXA curation activities for initial

411   characterization of allocated Ryugu particles. S.N., T. Okada., T.S., S.T., F.T., M.Y., S.W., and

412   Y.T. administered the project and acted as principal investigators. All authors contributed to the

413   data interpretation, commented on the earlier versions of the manuscript, and approved the final

414   version of the manuscript for submission.

415

416   **Competing interests**

417   The authors declare no competing interests.

418

419   **Figures and Captions**
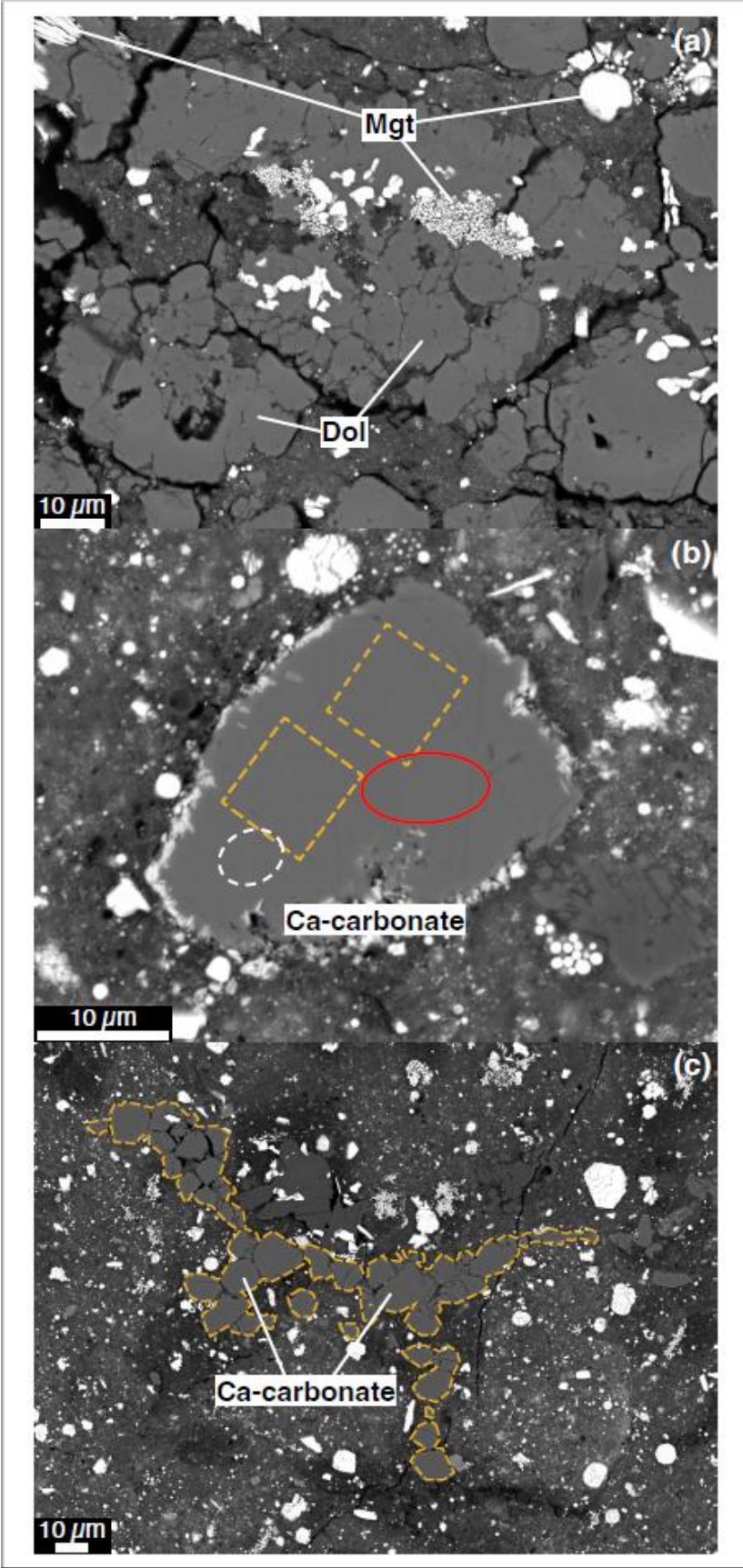
421 Figure 1. Backscattered electron (BSE) images of carbonate in Ryugu particles A0037 and C0009.

422 (a) Representative image of dolomite in A0037. Dol: dolomite, Mgt: magnetite. (b) The Ca-

423 carbonate 'Ca 2' in C0009 is isolated in the matrix and surrounded by an iron sulfide rim[45]. The

424 dotted white oval, red oval, and dashed yellow squares in (b) represent the size and location of the

425 oxygen, carbon, and Mn-Cr analysis pits, respectively. (c) Ca-carbonates in C0009 (outlined by a

426 yellow dotted line) are found as chains and clusters of individual grains with no rims[45].
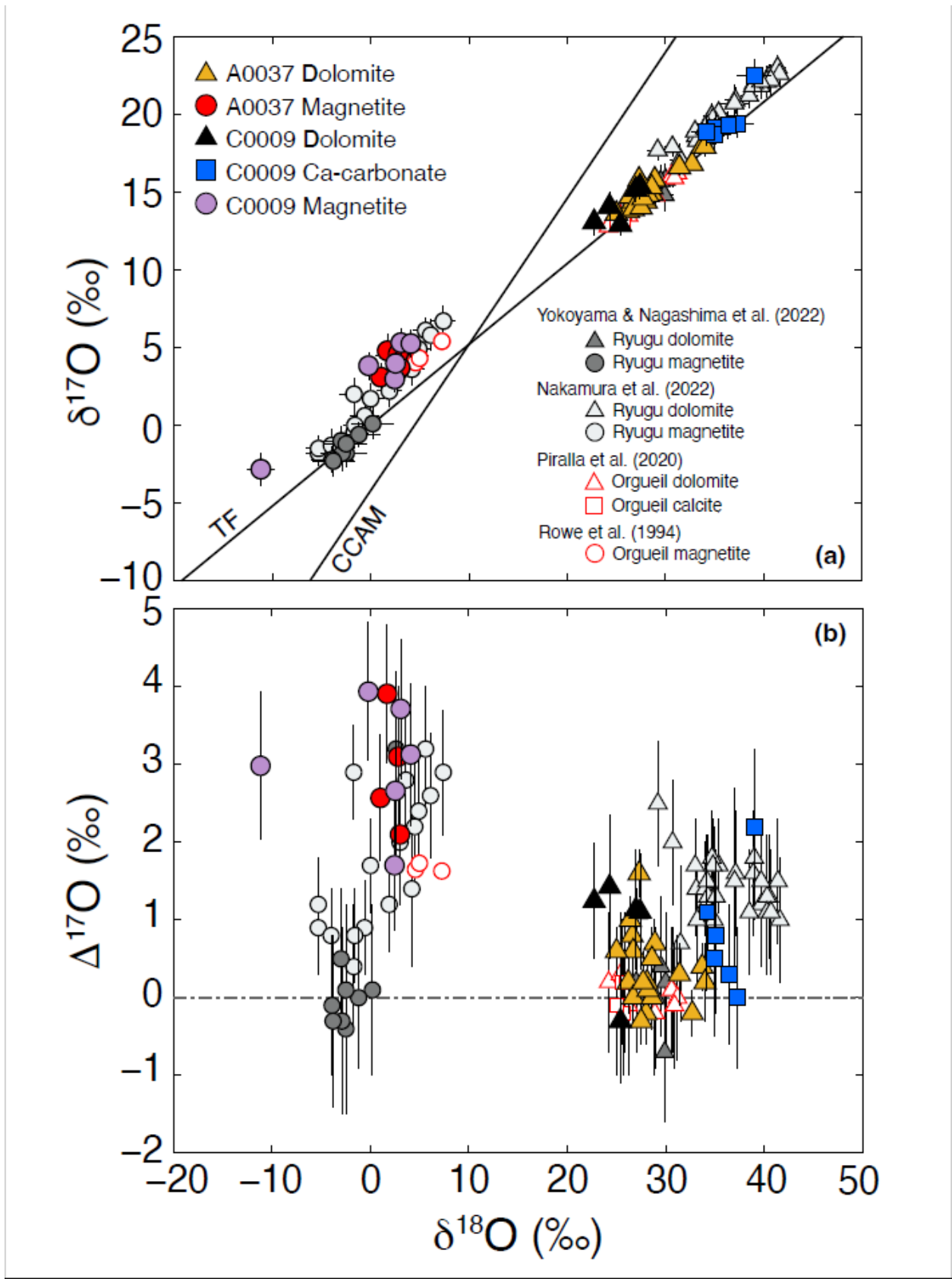
428   Figure 2. Oxygen isotopic compositions of carbonate and magnetite in Ryugu particles A0037 and

429   C0009. (a) three-isotope diagram relative to Standard Mean Ocean Water (SMOW). (b) $\Delta^{17}O$ vs.

430     $\delta^{18}O$ values. Errors are 2σ standard errors (see Methods). TF: terrestrial fractionation line, CCAM:

431   carbonaceous chondrite anhydrous minerals line. Also shown are in-situ dolomite and magnetite

432   from other Ryugu particles[4,5] (filled dark and light grey symbols), in-situ calcite and dolomite from

433   CI chondrite Orgueil[24] (open red triangles and squares), and bulk magnetite from CI chondrite

434   Orgueil (open red circles)[14].

435
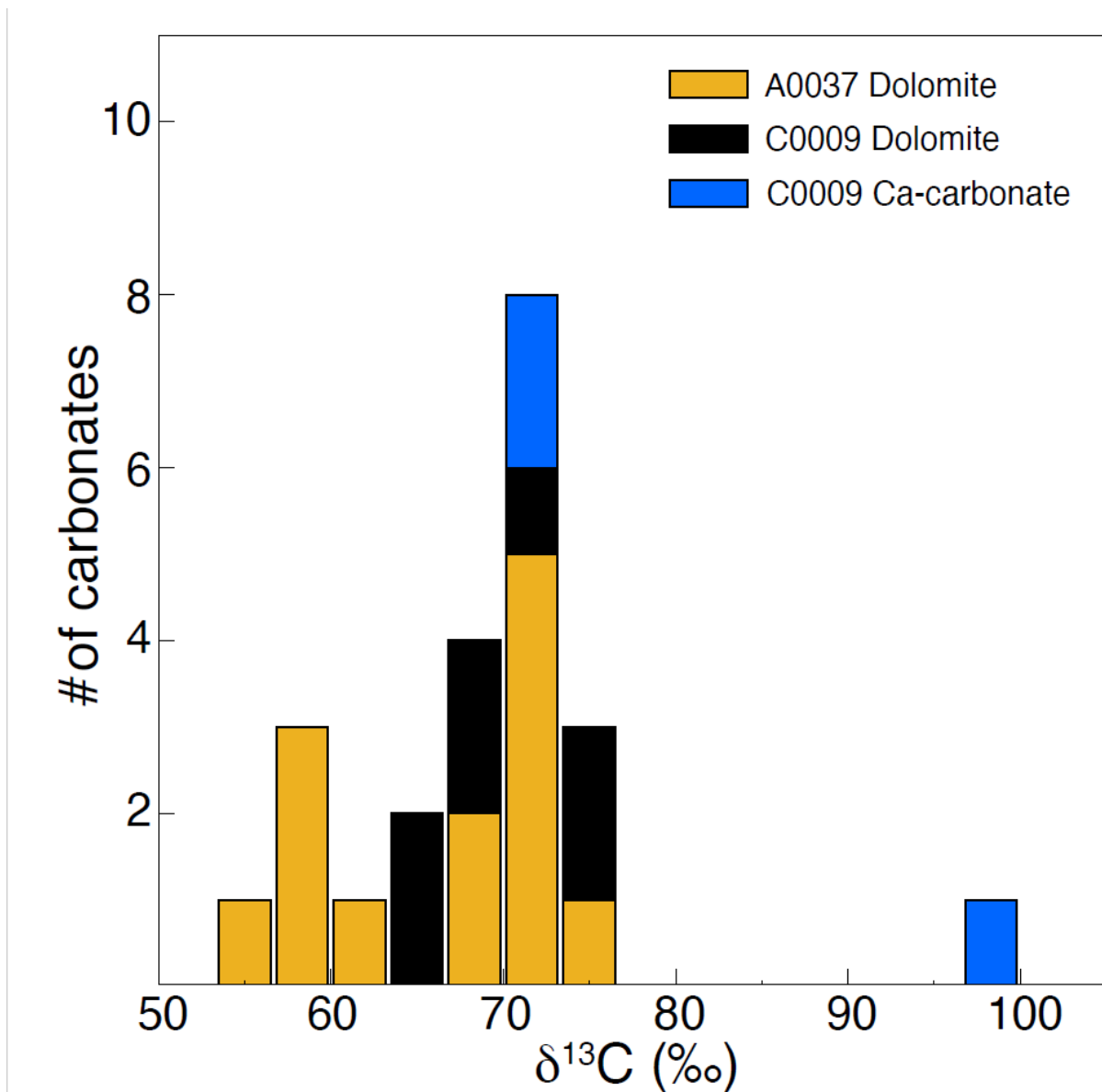
436 Figure 3. Stacked histogram of C isotopic compositions of carbonate in Ryugu particles A0037

437 and C0009 relative to Vienna PeeDee Belemnite (VPDB). The Ca-carbonate outlier at $\delta^{13}C = 97$

438 ‰ is 'Ca2' (see text).
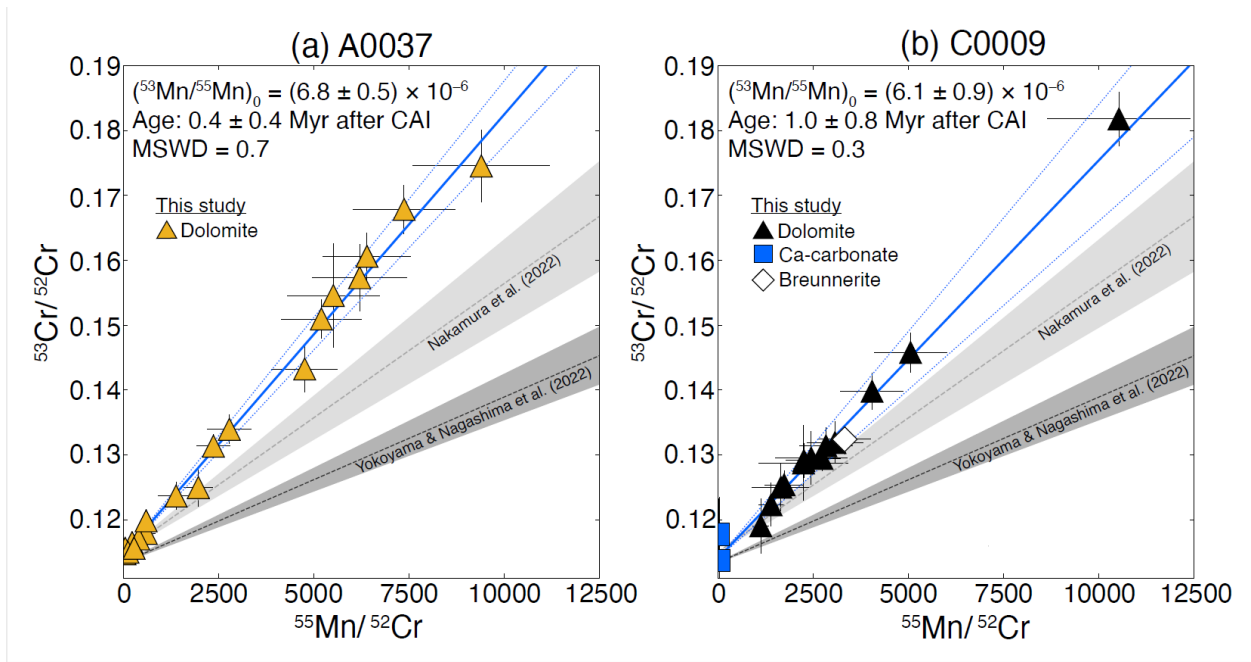
439

440 Figure 4. Mn-Cr isochrons for carbonates in Ryugu particles (a) A0037 and (b) C0009. Ages in

441 millions of years (Myr) are reported relative to an absolute CAI age of 4567.3 Ma[35] and anchored

442 to the D'Orbigny angrite age and $(^{53}Mn/^{55}Mn)_0$ (see text). Error bars ($\pm 2\sigma$) represent external and

443 internal errors summed in quadrature. The solid lines are least squares regression lines fitted to the

444 data, and dashed curves show 2σ uncertainties. Also shown are Mn-Cr isochrons reported for

445 dolomite from other Ryugu particles[4,5].

446
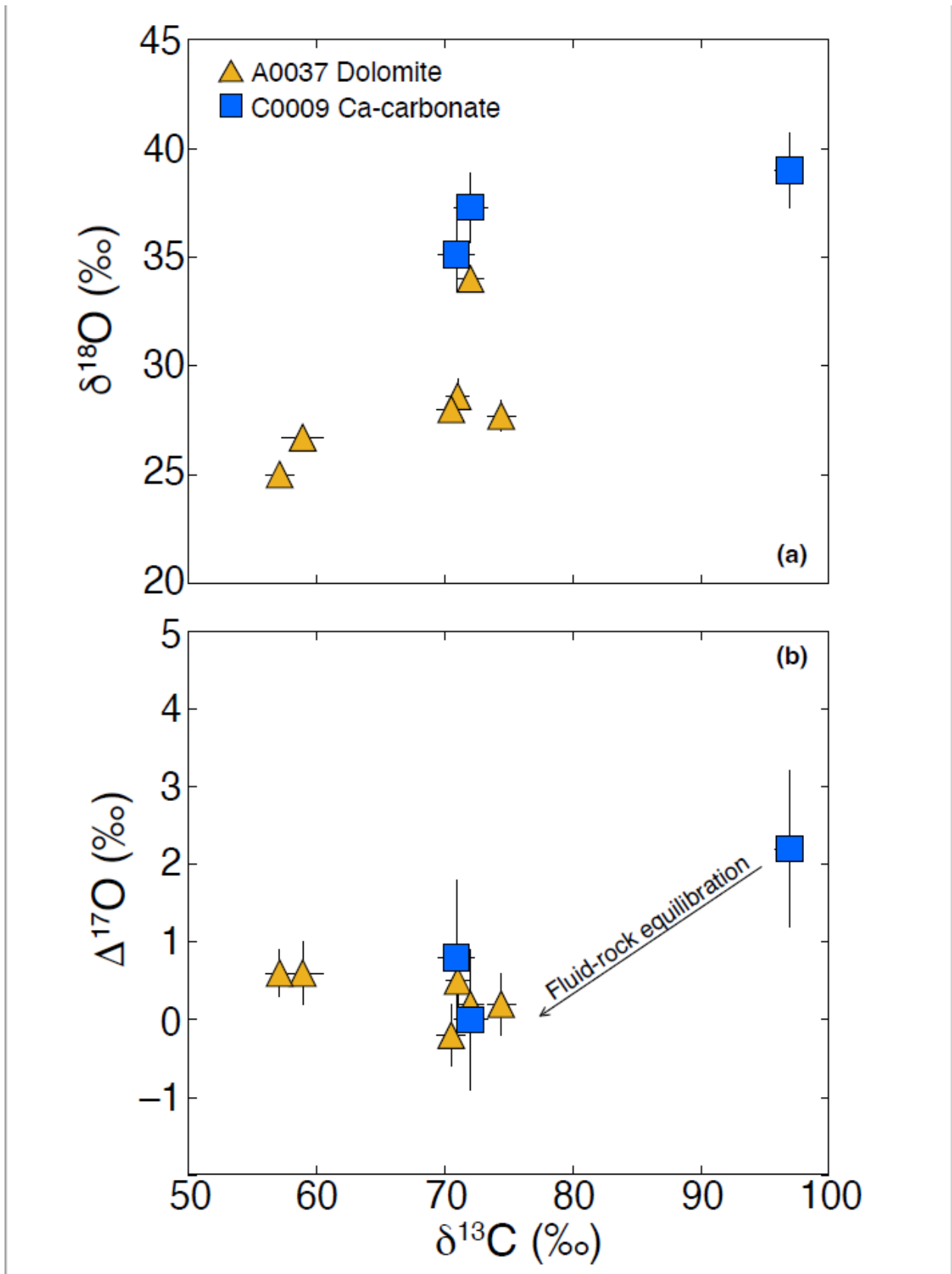
447   Figure 5. Carbon isotopic compositions (relative to VPDB) of Ryugu dolomite (yellow triangles)

448   and Ca-carbonate (blue squares) versus (a) $\delta^{18}O$ and (b) $\Delta^{17}O$ from the same carbonate grains.

449   Black arrow refers to the inferred direction of isotopic evolution over time (see Discussion), and

450   all error bars represent 2σ uncertainties (see Methods).

451

References

1. Yada, T. *et al.* Preliminary analysis of the Hayabusa2 samples returned from C-type asteroid Ryugu. *Nat. Astron.* **6**, 214–220 (2022) doi: 10.1038/s41550-021-01550-6.

2. Pilorget, C. *et al.* First compositional analysis of Ryugu samples by the MicrOmega hyperspectral microscope. *Nat. Astron.* **6**, 221–225 (2022) doi: 10.1038/s41550-021-01549-z.

3. Ito, M. *et al.* A pristine record of outer Solar System materials from asteroid Ryugu's returned sample. *Nat. Astron.* 1–9 (2022) doi:10.1038/s41550-022-01745-5.

4. Yokoyama, T. and Nagashima K. *et al.* Samples returned from the asteroid Ryugu are similar to Ivuna-type carbonaceous meteorites. *Science* **0**, eabn7850 (2022) doi: 10.1126/science.abn7850.

5. Nakamura, E. *et al.* On the origin and evolution of the asteroid Ryugu: A comprehensive geochemical perspective. *Proc. Jpn. Acad. Ser. B* **98**, 227–282 (2022) doi: 10.2183/pjab.98.015.

6. Greenwood, R. C. *et al.* Oxygen isotope evidence from asteroid Ryugu for early water delivery to Earth by CI chondrites. *Nat. Astron.* (In press).

7. King, A. J., Schofield, P. F., Howard, K. T. & Russell, S. S. Modal mineralogy of CI and CI-like chondrites by X-ray diffraction. *Geochim. Cosmochim. Acta* **165**, 148–160 (2015) doi: 10.1016/j.gca.2015.05.038.

8. Alfing, J., Patzek, M. & Bischoff, A. Modal abundances of coarse-grained (>5 μm) components within CI-chondrites and their individual clasts – Mixing of various lithologies on the CI parent body(ies). *Geochemistry* **79**, 125532 (2019) doi: 10.1016/j.chemer.2019.08.004.

475   9. Leshin, L. A., Rubin, A. E. & McKeegan, K. D. The oxygen isotopic composition of olivine

476   and pyroxene from CI chondrites. *Geochim. Cosmochim. Acta* **61**, 835–845 (1997) doi:

477   10.1016/S0016-7037(96)00374-2.

478   10. Clayton, R. N. & Mayeda, T. K. Oxygen isotope studies of carbonaceous chondrites.

479   *Geochim. Cosmochim. Acta* **63**, 2089–2104 (1999) doi: 10.1016/S0016-7037(99)00090-3.

480   11. Fujiya, W., Sugiura, N., Sano, Y. & Hiyagon, H. Mn–Cr ages of dolomites in CI chondrites

481   and the Tagish Lake ungrouped carbonaceous chondrite. *Earth Planet. Sci. Lett.* **362**, 130–

482   142 (2013) doi: 10.1016/j.epsl.2012.11.057.

483   12. Visser, R., John, T., Whitehouse, M. J., Patzek, M. & Bischoff, A. A short-lived ^{26}Al

484   induced hydrothermal alteration event in the outer solar system: Constraints from Mn/Cr

485   ages of carbonates. *Earth Planet. Sci. Lett.* **547**, 116440 (2020) doi:

486   10.1016/j.epsl.2020.116440.

487   13. Clayton, R. N. & Mayeda, T. K. The oxygen isotope record in Murchison and other

488   carbonaceous chondrites. *Earth Planet. Sci. Lett.* **67**, 151–161 (1984) 10.1016/0012-

489   821X(84)90110-9.

490   14. Rowe, M. W., Clayton, R. N. & Mayeda, T. K. Oxygen isotopes in separated components of

491   CI and CM meteorites. *Geochim. Cosmochim. Acta* **58**, 5341–5347 (1994) doi:

492   10.1016/0016-7037(94)90317-4.

493   15. Tyra, M. A., Farquhar, J., Guan, Y. & Leshin, L. A. An oxygen isotope dichotomy in CM2

494   chondritic carbonates—A SIMS approach. *Geochim. Cosmochim. Acta* **77**, 383–395 (2012)

495   doi: 10.1016/j.gca.2011.10.003.

496   16. Lee, M. R., Sofe, M. R., Lindgren, P., Starkey, N. A. & Franchi, I. A. The oxygen isotope

497   evolution of parent body aqueous solutions as recorded by multiple carbonate generations in

498   the Lonewolf Nunataks 94101 CM2 carbonaceous chondrite. *Geochim. Cosmochim. Acta*

499   **121**, 452–466 (2013) doi: 10.1016/j.gca.2013.07.010.

500   17. Lee, M. R., Lindgren, P. & Sofe, M. R. Aragonite, breunnerite, calcite and dolomite in the

501   CM carbonaceous chondrites: High fidelity recorders of progressive parent body aqueous

502   alteration. *Geochim. Cosmochim. Acta* **144**, 126–156 (2014) doi: 10.1016/j.gca.2014.08.019.

503   18. Fujiya, W. *et al.* Comprehensive study of carbon and oxygen isotopic compositions, trace

504   element abundances, and cathodoluminescence intensities of calcite in the Murchison CM

505   chondrite. *Geochim. Cosmochim. Acta* **161**, 101–117 (2015) doi: 10.1016/j.gca.2015.04.010.

506   19. Tyra, M., Brearley, A. & Guan, Y. Episodic carbonate precipitation in the CM chondrite

507   ALH 84049: An ion microprobe analysis of O and C isotopes. *Geochim. Cosmochim. Acta*

508   **175**, 195–207 (2016) doi: 10.1016/j.gca.2015.10.034.

509   20. Vacher, L. G., Marrocchi, Y., Villeneuve, J., Verdier-Paoletti, M. J. & Gounelle, M.

510   Petrographic and C & O isotopic characteristics of the earliest stages of aqueous alteration of

511   CM chondrites. *Geochim. Cosmochim. Acta* **213**, 271–290 (2017) doi:

512   10.1016/j.gca.2017.06.049.

513   21. Verdier-Paoletti, M. J. *et al.* Oxygen isotope constraints on the alteration temperatures of

514   CM chondrites. *Earth Planet. Sci. Lett.* **458**, 273–281 (2017) doi:

515   10.1016/j.epsl.2016.10.055.

516   22. Vacher, L. G., Marrocchi, Y., Villeneuve, J., Verdier-Paoletti, M. J. & Gounelle, M.

517   Collisional and alteration history of the CM parent body. *Geochim. Cosmochim. Acta* **239**,

518   213–234 (2018) doi: 10.1016/j.gca.2018.08.006.

519   23. Telus, M., Alexander, C. M. O., Hauri, E. H. & Wang, J. Calcite and dolomite formation in

520   the CM parent body: Insight from in situ C and O isotope analyses. *Geochim. Cosmochim.*

521   *Acta* **260**, 275–291 (2019) doi: 10.1016/j.gca.2019.06.012.

522   24. Piralla, M. *et al.* Primordial water and dust of the Solar System: Insights from in situ oxygen

523   measurements of CI chondrites. *Geochim. Cosmochim. Acta* **269**, 451–464 (2020) doi:

524   10.1016/j.gca.2019.10.041.

525   25. Bischoff, A. *et al.* The old, unique C1 chondrite Flensburg – Insight into the first processes

526   of aqueous alteration, brecciation, and the diversity of water-bearing parent bodies and

527   lithologies. *Geochim. Cosmochim. Acta* **293**, 142–186 (2021) doi:

528   10.1016/j.gca.2020.10.014.

529   26. Sakamoto, N. *et al.* Remnants of the Early Solar System Water Enriched in Heavy Oxygen

530   Isotopes. *Science* (2007) doi:10.1126/science.1142021.

531   27. Liu, M.-C. *et al.* Incorporation of 16O-rich anhydrous silicates in the protolith of hihgly

532   hydrated asteroid Ryugu. *Nat. Astron.* **6**, 1172-1177 (2022) doi: 10.1038/s41550-022-01762-

533   4.

534   28. Alexander, C. M. O., Fogel, M., Yabuta, H. & Cody, G. D. The origin and evolution of

535   chondrites recorded in the elemental and isotopic compositions of their macromolecular

536   organic matter. *Geochim. Cosmochim. Acta* **71**, 4380–4403 (2007) doi:

537   10.1016/j.gca.2007.06.052.

538   29. Sephton, M. A., Pillinger, C. T. & Gilmour, I. Aromatic moieties in meteoritic

539   macromolecular materials: analyses by hydrous pyrolysis and $\delta^{13}C$ of individual compounds.

540   *Geochim. Cosmochim. Acta* **64**, 321–328 (2000) doi: 10.1016/S0016-7037(99)00282-3.

541   30. Hässig, M. *et al.* Isotopic composition of CO_2 in the coma of 67P/Churyumov-Gerasimenko

542   measured with ROSINA/DFMS. *Astron. Astrophys.* **605**, A50 (2017) doi: 10.1051/0004-

543   6361/201630140.

544   31. Fujiya, W., Aoki, Y., Ushikubo, T., Hashizume, K. & Yamaguchi, A. Carbon isotopic

545   evolution of aqueous fluids in CM chondrites: Clues from in-situ isotope analyses within

546   calcite grains in Yamato-791198. *Geochim. Cosmochim. Acta* **274**, 246–260 (2020) doi:

547   10.1016/j.gca.2020.02.003.

548   32. Guo, W. & Eiler, J. M. Temperatures of aqueous alteration and evidence for methane

549   generation on the parent bodies of the CM chondrites. *Geochim. Cosmochim. Acta* **71**, 5565–

550   5575 (2007) doi: 10.1016/j.gca.2007.07.029.

551   33. Alexander, C. M. O., Bowden, R., Fogel, M. L. & Howard, K. T. Carbonate abundances and

552   isotopic compositions in chondrites. *Meteorit. Planet. Sci.* **50**, 810–833 (2015) doi:

553   10.1111/maps.12410.

554   34. Fujiya, W. *et al.* Migration of D-type asteroids from the outer Solar System inferred from

555   carbonate in meteorites. *Nat. Astron.* 1 (2019) doi:10.1038/s41550-019-0801-4.

556   35. Zito, K. L., McKeegan, K. D., Kerridge, J. F., Hutcheon, I. D. & Leshin, L. A. Aqueous

557   Alteration on the CI Parent Body: Evidence from Oxygen and Carbon Isotopic Studies of

558   Single Carbonate Grains from Orgueil. *Meteorit. Planet. Sci. Suppl.* **33**, 171 (1998).

559   36. Fujiya, W., Sugiura, N., Hotta, H., Ichimura, K. & Sano, Y. Evidence for the late formation

560   of hydrous asteroids from young meteoritic carbonates. *Nat. Commun.* **3**, 627 (2012) doi:

561   10.1038/ncomms1635.

562   37. Sugiura, N. & Ichimura, K. Mn/Cr relative sensitivity factors for synthetic calcium carbonate

563   measured with a NanoSIMS ion microprobe. *Geochem. J.* **44**, e11-316 (2010) doi:

564   10.2343/geochemj.1.0089.

565   38. Steele, R. C. J., Heber, V. S. & McKeegan, K. D. Matrix effects on the relative sensitivity

566   factors for manganese and chromium during ion microprobe analysis of carbonate:

567   Implications for early Solar System chronology. *Geochim. Cosmochim. Acta* **201**, 245–259

568   (2017) doi: 10.1016/j.gca.2016.10.046.

569   39. McCain, K. A., Liu, M.-C. & McKeegan, K. D. Calibration of matrix-dependent biases in

570   isotope and trace element analyses of carbonate minerals. *J. Vac. Sci. Technol. B* **38**, 044005

571   (2020) doi: 10.1116/6.0000111.

572   40. McKibbin, S. J., Ireland, T. R., Amelin, Y. & Holden, P. Mn–Cr dating of Fe- and Ca-rich

573   olivine from 'quenched' and 'plutonic' angrite meteorites using Secondary Ion Mass

574   Spectrometry. *Geochim. Cosmochim. Acta* **157**, 13–27 (2015) doi:

575   10.1016/j.gca.2015.02.019.

576   41. Brennecka, G. A. & Wadhwa, M. Uranium isotope compositions of the basaltic angrite

577   meteorites and the chronological implications for the early Solar System. *Proc. Natl. Acad.*

578   *Sci.* **109**, 9299–9303 (2012) doi: 10.1073/pnas.1114043109.

579   42. Amelin, Y. U–Pb ages of angrites. *Geochim. Cosmochim. Acta* **72**, 221–232 (2008) doi:

580   10.1016/j.gca.2007.09.034.

581   43. Amelin, Y. *et al.* U-Pb chronology of the Solar System's oldest solids with variable

582        $^{238}U/^{235}U$. *Earth Planet. Sci. Lett.* **300**, 343–350 (2010) doi: 10.1016/j.epsl.2010.10.015.

583   44. Jilly, C. E. *et al.* ^{53}Mn-^{53}Cr dating of aqueously formed carbonates in the CM2 lithology of

584   the Sutter's Mill carbonaceous chondrite. *Meteorit. Planet. Sci.* **49**, 2104–2117 (2014) doi:

585   10.1111/maps.12305.

586   45. Yamaguchi, A. *et al.* Fresh insight into geological evolution of C-type asteroids from Ryugu

587   particles. *Nat. Astron.* (In press).

588   46. Hayles, J., Gao, C., Cao, X., Liu, Y. & Bao, H. Theoretical calibration of the triple oxygen

589   isotope thermometer. *Geochim. Cosmochim. Acta* **235**, 237–245 (2018) doi:

590   10.1016/j.gca.2018.05.032.

591   47. Horita, J. Oxygen and carbon isotope fractionation in the system dolomite–water–CO_2 to

592   elevated temperatures. *Geochim. Cosmochim. Acta* **129**, 111–124 (2014) doi:

593   10.1016/j.gca.2013.12.027.

594   48. Saccocia, P. J., Seewald, J. S. & Shanks, W. C. Oxygen isotope fractionation in the

595   portlandite–water and brucite–water systems from 125 to 450°C, 50MPa. *Geochim.*

596   *Cosmochim. Acta* **169**, 137–151 (2015) doi: 10.1016/j.gca.2015.07.017.

597   49. Zolensky, M., Barrett, R. & Browning, L. Mineralogy and composition of matrix and

598   chondrule rims in carbonaceous chondrites. *Geochim. Cosmochim. Acta* **57**, 3123–3148

599   (1993) doi: 10.1016/0016-7037(93)90298-B.

600   50. McCain, K. A., Young, E. D. & Manning, C. E. CM Carbonates Should Be Old: Insights

601   from Parent Body Thermal Modeling. in vol. 48 2181 (2017).

602   51. Zhou, Q. *et al.* SIMS Pb–Pb and U–Pb age determination of eucrite zircons at < 5 μm scale

603   and the first 50 Ma of the thermal history of Vesta. *Geochim. Cosmochim. Acta* **110**, 152–

604   175 (2013) doi: 10.1016/j.gca.2013.02.016.

605   52. Watanabe, S. *et al.* Hayabusa2 arrives at the carbonaceous asteroid 162173 Ryugu—A

606   spinning top–shaped rubble pile. *Science* (2019) doi:10.1126/science.aav8032.

607   53. Tomioka, N. *et al.* Calibrating the shock regime experienced by the regolith particles of

608   hydrated asteroid Ryugu. *Nat. Astron.* (In press).

609   54. Kleine, T. *et al.* The Non-carbonaceous–Carbonaceous Meteorite Dichotomy. *Space Sci.*

610   *Rev.* **216**, 55 (2020) doi: 10.1007/s11214-020-00675-w.

611   55. Kruijer, T. S., Burkhardt, C., Budde, G. & Kleine, T. Age of Jupiter inferred from the

612   distinct genetics and formation times of meteorites. *Proc. Natl. Acad. Sci.* **114**, 6712–6716

613   (2017) doi: 10.1073/pnas.1704461114.

614   56. Sugiura, N. & Fujiya, W. Correlated accretion ages and ε^{54}Cr of meteorite parent bodies and

615   the evolution of the solar nebula. *Meteorit. Planet. Sci.* **49**, 772–787 (2014) doi:

616   10.1111/maps.12292.

617   57. Desch, S. J., Kalyaan, A. & Alexander, C. M. O. The Effect of Jupiter's Formation on the

618   Distribution of Refractory Elements and Inclusions in Meteorites. *Astrophys. J. Suppl. Ser.*

619   **238**, 11 (2018) doi: 10.3847/1538-4365/aad95f.

620   58. Śliwiński, M. G. *et al.* Secondary Ion Mass Spectrometry Bias on Isotope Ratios in

621   Dolomite–Ankerite, Part I: δ^{18}O Matrix Effects. *Geostand. Geoanalytical Res.* **40**, 157–172

622   (2016) doi: 10.1111/j.1751-908X.2015.00364.x.

623   59. Śliwiński, M. G. *et al.* Secondary Ion Mass Spectrometry Bias on Isotope Ratios in

624   Dolomite–Ankerite, Part II: δ^{13}C Matrix Effects. *Geostand. Geoanalytical Res.* **40**, 173–184

625   (2016) doi: 10.1111/j.1751-908X.2015.00380.x.

626   60. Papanastassiou, D. A. Chromium isotopic anomalies in the Allende meteorite. *Astrophys. J.*

627   **308**, L27–L30 (1986) doi: 10.1086/184737.

628   61. York, D., Evensen, N. M., Martínez, M. L. & De Basabe Delgado, J. Unified equations for

629   the slope, intercept, and standard errors of the best straight line. *Am. J. Phys.* **72**, 367–375

630   (2004) doi: 10.1119/1.1632486.

631

632 **Supplementary Materials**

633 **Mn-Cr carbonate standard production and characterization**

634   Natural carbonate minerals from the UCLA and the Field Museum of Natural History

635 (FMNH) mineral collections which span the range of Fe contents found in Ryugu carbonate (0–8

636 mol% $FeCO_3$ for dolomite and 0–40 mol% $FeCO_3$ for magnesite) were embedded in Field's metal

637 and/or indium in the center of aluminum disks. Fragments of San Carlos Olivine and the NIST 612

638 and 614 glasses were mounted in the same disks for use as concentration standards to calibrate the

639 implant fluence. The mount was coated with 20 nm carbon to ensure conductivity and prevent

640 charging during ion implantation. All mounts were implanted with a 185 KeV $^{52}Cr^+$ ion beam at a

641 nominal fluence of 4×10^{13} ions/cm^2 rastered over the entire surface. A mass filter was used to

642 separate $^{52}Cr^+$ and $^{53}Cr^+$ after Cr ionization, ensuring that only $^{52}Cr^+$ was implanted. No evidence

643 of implanted $^{53}Cr^+$ (e.g. an increase and then decay in intensity similar in shape to the $^{52}Cr^+$

644 intensity) was observed in any of our implanted materials. Ion implantation was carried out by

645 CuttingEdge Ions.

646   To determine the implanted $^{52}Cr^+$ fluence and RSF for each terrestrial carbonate, the NIST

647 glasses, San Carlos Olivine, and terrestrial carbonates were sputtered using a 2nA O_3^- primary

648 beam focused into a ~3 μm spot rastered over 50×50 μm^2 areas. A field aperture was inserted into

649 an ion image plane to restrict the collected ions to the central 15×15 μm^2 area of each raster

650 square. An 80 μm entrance slit width was used. Secondary ions of $^{44}Ca^+$, $^{52}Cr^+$, $^{53}Cr^+$, and $^{55}Mn^+$

651 were counted using an electron multiplier in monocollection mode. Prior to analysis, the C coating

652 was removed without the use of polishing compound and replaced with a 30 nm layer of gold to

653 prevent charging during the ion probe analysis.

654   The implanted fluence and RSF of each terrestrial carbonate were determined following

655   methods previously described[1]. The calibrated implanted fluence determined using the NIST

656   glasses was $(4.57 \pm 0.05) \times 10^{13}$ ions/cm^2 (2SE). For depth profiles of calcite and dolomite, surface

657   ^{52}Cr contamination cannot be completely accounted for by simply measuring the background ^{53}Cr

658   intensity, due to the low background Cr abundance in these minerals and fast sputtering rates

659   observed in depth profiles of these materials (shown in Supplementary Figure 1). Instead, the ^{52}Cr

660   background was corrected for by estimating the expected position and width of the implantation

661   peak, which can be well-modeled by a Gaussian distribution, in each mineral with the SRIM

662   software[2] (Supplementary Figure 1, red line). As shown in the right panel of Supplementary Figure

663   1, the modeled implantation peak (red line) fits the measured ^{53}Cr-corrected ^{52}Cr intensities (thin

664   black line) well at depths below 50 nm after which contamination is no longer significant.

665   Therefore, we used the ^{52}Cr intensity predicted by the Gaussian distribution as the corrected

666   intensity for the upper 50 nm of the profile for profiles showing signs of surface contamination

667   and used the measured intensities for the remainder of the profile. For calcite and dolomite,

668   correction for surface contamination resulted in changes to the measured RSF by 20–30%.

669   Analyses of magnesite, NIST glass, and olivine were not affected by surface contamination due to

670   the higher natural Cr abundance of these standard materials.

671

Variation of RSF with ion probe spot geometry

673   To ascertain that the RSF of the ^{55}Mn/^{52}Cr ratio obtained by depth profiling can be applied

674   to the Ryugu data acquired with a static spot[3], we compared the RSF results on non-implanted and

675   implanted San Carlos olivine measured in spot and depth profiling modes, respectively. The true

676   ^{55}Mn/^{52}Cr ratio of our San Carlos Olivine standard was found to be 9.2 ± 0.7 by EPMA. We found

677 that the RSF values acquired under the two conditions were identical within error (Supplementary

678 Figure 2), and we can therefore use the RSF values for dolomite and magnetite obtained in raster

679 mode to correct the $^{55}Mn/^{52}Cr$ ratio of our spot analyses.

680   The RSF values obtained from depth profiling of natural materials are given in

681 Supplementary Table 6. The RSF is calculated as

$$(3)\ RSF\ =\ \frac{C_{55Mn}DA_{52Cr+}}{I_{55Mn}Ft}$$

683 where C_{55Mn} represents the concentration of ^{55}Mn as determined by EPMA (shown in

684 Supplementary Table 6), D represents the depth of the rastered area, A_{52Cr+} represents the total

685 number of counts of implanted $^{52}Cr^+$ (as defined above), I_{55Mn} represents the measured signal

686 intensity of $^{55}Mn^+$ during the depth profile, F represents the fluence of ^{52}Cr implanted as calculated

687 above, and t represents the total duration of the profile. The depth of the rastered area was

688 determined using the Dektak XT stylus profilometer at the Molecular Materials Research Center

689 at the California Institute of Technology. The values used to calculate the RSF for each depth

690 profile are given in Supplementary Table 7.

691   The relationship of the RSF with the $FeCO_3$ content of dolomite is shown in supplementary

692 Figure 3, and can be fit to an exponential using the curve_fit function from the SciPy Optimization

693 module[4]:

$$(4)\ RSF\ =\ 0.235 * e^{-0.345x}\ +\ 0.705$$

695 where x refers to the Fe content of the dolomite in Mol %. Due to the large errors associated with

696 MS1305, this point was not included during calculation of the fit. As shown in Supplementary

697 Table 1, dolomite in Ryugu has a restricted range of Fe content, with an average of 3.5 mol%

698 $FeCO_3$. This value corresponds to an RSF value of 0.8. The Fe content of Ryugu dolomites show

699 only small departures from the average Fe abundance, which would lead to RSF variations well

700 within our errors. Therefore, we use the value of 0.8 obtained for the average Ryugu dolomite

701 composition for all analyses of Ryugu dolomite.

702 The relationship of the RSF with the $FeCO_3$ content of magnesite is shown in

703 Supplementary Figure 4. The data were fit to a linear relationship using the 'fit_bivariate' python

704 module, an implementation of the York et al. (2004) line fitting algorithm[5]. For the single

705 magnesite analysis in C0009, the magnesite has an $FeCO_3$ content of approximately 14 mol%

706 derived from EDS analyses. Using the equation derived from the line fitting algorithm, we obtain

707 an RSF value of 0.86.

708

709 **Magnetite-calcite equilibrium calculation**

710 The formation temperature is calculated under the assumption that Ca-carbonate 'Ca 2' and

711 magnetite were in equilibrium with waters of identical oxygen isotopic composition. Using the

712 range of magnetite compositions observed in C0009 and A0037 ($\delta^{18}O$ from −11.2 to 4.1 ‰) and

713 the uncertainty related to the composition of 'Ca 2' ($\delta^{18}O = 39 \pm 1.7$‰ (2SE)), we inferred 1000

714 ln $\alpha_{Cal-Mgt}$ values which ranged from 51.9 to 33.2‰. Calcite fractionation factors for 'Ca 2' were

715 adopted due to the strong resemblance in petrology and O isotopic composition of this target to

716 Type 1 calcite in CM chondrites. We note that values of 1000 ln $\alpha_{Cal-Mgt}$ below 35.7 ‰ correspond

717 to temperatures below the freezing point of water, from which it is possible to infer that some

718 Ryugu magnetite formed out of equilibrium with 'Ca 2' despite having similar values of $\Delta^{17}O$.

719 We assume no significant effect of crystallographic orientation on the mass fractionation

720 of oxygen isotopic measurements of magnetite[6]. In principle, this could affect the accuracy of our

721 measured $\delta^{18}O$ values of magnetite by up to 3‰, but would not affect measurements of $\Delta^{17}O$. Any

722 shift in the $\delta^{18}O$ value of magnetite would affect the $\alpha_{Cal-Mgt}$ inferred using the magnetite and calcite

723   pair, thereby affecting the temperature calculation. However, we note that magnetite-water

724   fractionation has a weak temperature dependence relative to calcite-water fractionation. Therefore,

725   a crystallographic orientation effect for $\delta^{18}O$ of would not strongly affect the inferred temperature

726   range.

727   We estimated the formation temperature of calcite and magnetite to be 0–20 °C based on

728   fractionation factors for the calcite-water and magnetite-water systems derived from theoretical

729   calculations performed by Hayles et al. (2018)[7]. Some previous studies of magnetite-carbonate

730   equilibrium in carbonaceous chondrites have used other fractionation factors for the magnetite-

731   water equilibrium[8,9]. If we use the magnetite-water fractionation factors calculated in Zheng et al.

732   1995, along with experimentally-derived calcite-water fractionation factors[10], we obtain a

733   formation temperature of 0–47 °C. Experimental data for the magnetite-water equilibrium

734   fractionation are available only at temperatures above 300 °C[11]. Therefore, we have elected to use

735   the most recent theoretical predictions of the equilibrium fractionation between magnetite and

736   water at low temperature in our calculations.

737

738   **Dolomite-phyllosilicate equilibrium calculation**

739   We estimated the formation temperature of phyllosilicate and dolomite to be 88–240 °C

740   using dolomite-H_2O and brucite-H_2O fractionation factors[12,13] which have been experimentally

741   determined at the relevant low temperatures. Relatively few hydrated Mg-rich minerals have

742   reliable fractionation factors measured at low temperature. While other minerals (e.g. serpentine)

743   would provide better fits to the mineralogy observed in the Ryugu matrix, their mineral-H_2O

744   fractionations are not well constrained at the relevant temperatures. Therefore, we elect to use the

745   brucite-H_2O fractionation factor. The range of temperatures inferred by this calculation is

746   extremely wide due to the uncertainty in the bulk phyllosilicate $\delta^{18}O$ composition, so variation in

747   the phyllosilicate-water fractionation factors is likely within this range of inferred temperatures.

748

MS1317j@15
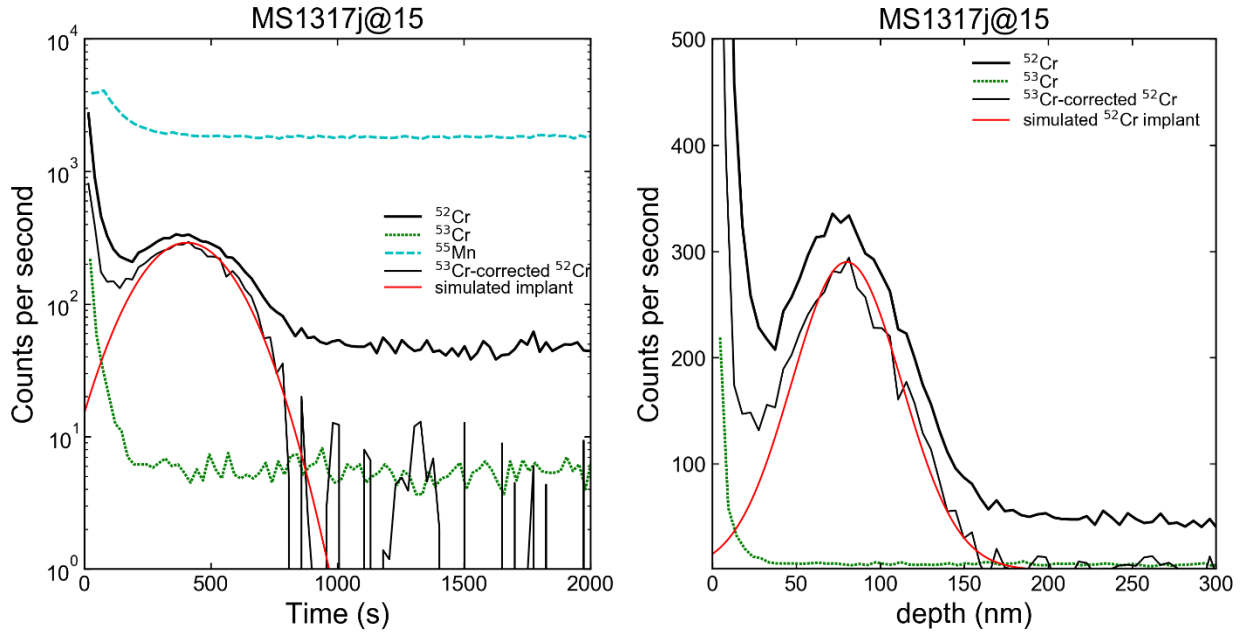
terrestrial dolomite 1317J plotted against the time elapsed during the depth profile (left) and the depth below the sample surface (right). The left panel is shown with count rates on a logarithmic scale, and the right with count rates on a linear scale for comparison. The heavy black line represents the intensity of $^{52}Cr^+$ including the implanted Cr and the background Cr in the NIST glass. The dotted green line represents the intensity of the background $^{53}Cr^+$ during the profile. The dashed blue line represents the intensity of $^{55}Mn^+$ during the profile. The thin black line represents the intensity of $^{52}Cr^+$ when background-corrected only by the $^{53}Cr^+$ intensity. The red line represents the $^{52}Cr^+$ implantation peak as simulated by the SRIM software.

San Carlos Olivine

Depth profiling RSF

60 s, 8 μm presputter, 5 μm analysis

3 EM condition

120 s, 8 μm presputter, 5 μm analysis

60 s, 4 μm presputter, 2 μm analysis
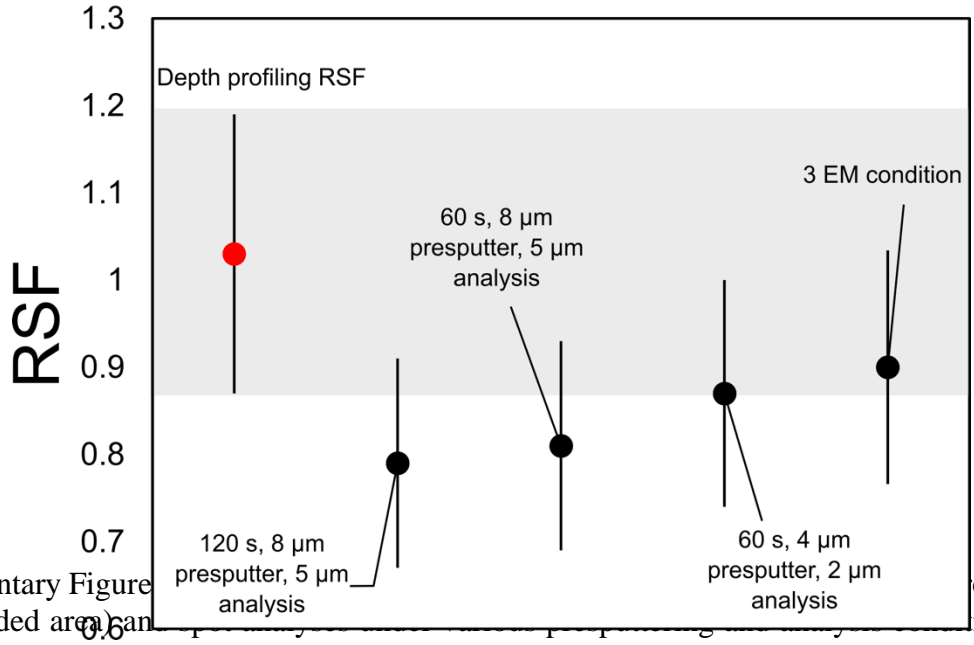
Supplementary Figure ... ofiling (red point, shaded area) ... ions (black circles). Error bars represent 2SE.

801
802
803
804
805
806
807
808
809
810
811
812
813
814
815
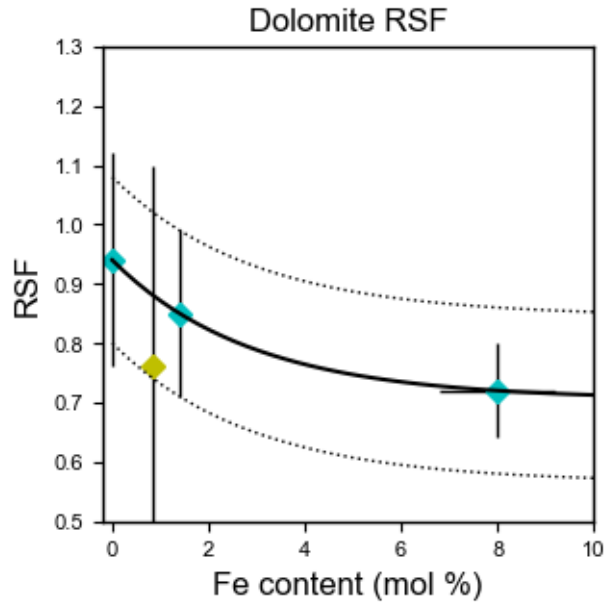
Dolomite RSF

816   Supplementary Figure 3.   sition of dolomite.
817   The black line is the expo   ent 2 SE.
818

819
820
821
822
823
824
825
826
827
828
829
830
831
832
833
834

Magnesite RSF

$RSF = 0.95\,(\pm 0.12) - FeCO_3 \times 0.007\,(\pm 0.006)$
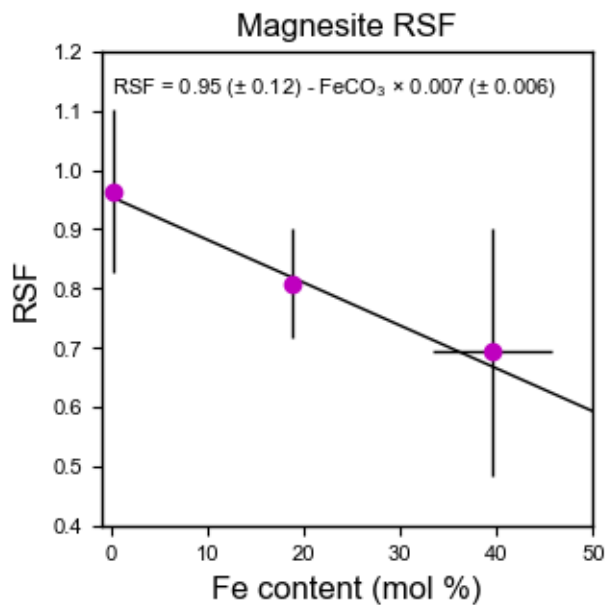
835 Supplementary Figure 4. RSF values of magnesite versus the $FeCO_3$ composition of magnesite,
836 errors 2SE. The black line is the best fit line printed on the plot.
837

Supplementary Table 1. Oxygen-isotope compositions of carbonates in A0037 and C0009.

Particles	Mineral	Spot #	$\delta^{17}O$	2σ	$\delta^{18}O$	2σ	$\Delta^{17}O$	2σ	$FeCO_3$*	$MnCO_3$*	OH^- intensity (counts/second)
A0037	Dolomite	A37_3oxy3FCs@1	14.8	0.4	28.1	0.4	0.2	0.4	4.1	4.4	1.85×10^7
		A37_3oxy3FCs@2	13.8	0.4	26.2	0.4	0.2	0.4	3.8	2.7	1.03×10^7
		A37_3oxy3FCs@3	14.7	0.4	26.6	0.4	0.8	0.4	4.1	2.3	1.79×10^7
		A37_3oxy3FCs@4	15.1	0.4	27.0	0.4	1.1	0.3	3.9	4.0	0.64×10^7
		A37_3oxy3FCs@6	14.4	0.5	26.7	0.4	0.6	0.4	4.6	4.7	0.98×10^7
		A37_3oxy3FCs@7	14.7	0.4	26.4	0.4	1.0	0.3	4.3	5.8	1.87×10^7
		A37_3oxy3FCs@8	16.8	0.3	32.7	0.4	–0.2	0.3	3.2	5.3	1.67×10^7
		A37_3oxy3FCs@9	16.6	0.5	31.4	0.4	0.3	0.4	4.1	3.7	1.98×10^7
		A37_3oxy3FCs@10	14.4	0.4	28.0	0.4	–0.2	0.4	3.8	4.1	0.93×10^7
		A37_3oxy3FCs@11	17.9	0.3	33.7	0.4	0.4	0.3	3.2	5.3	1.67×10^7
		A37_3oxy3FCs@13	13.6	0.4	25.0	0.4	0.6	0.3	4.0	6.8	1.42×10^7
		A37_3oxy3FCs@14	15.8	0.4	28.9	0.4	0.7	0.3	4.0	3.9	1.70×10^7
		A37_3oxyFCEMFC@1	13.9	0.4	26.7	0.6	0.0	0.3	3.0	5.7	2.00×10^6
		A37_3oxyFCEMFC@2	15.8	0.5	27.3	0.7	1.6	0.3	4.3	5.8	1.50×10^6
		A37_3oxyFCEMFC@4	14.9	0.3	28.6	0.6	0.0	0.4	3.8	5.7	1.52×10^6
		A37_3oxyFCEMFC@5	17.9	0.6	34.0	0.6	0.2	0.5	4.0	3.9	3.60×10^6
		A37_3oxyFCEMFC@6	14.8	0.5	28.2	0.6	0.1	0.4	4.0	3.9	2.95×10^6
		A37_3oxyFCEMFC@7	14.0	0.4	27.5	0.7	–0.3	0.3	4.0	2.4	7.50×10^6
		A37_3oxyFCEMFC@8	15.3	0.5	28.6	0.8	0.5	0.4	3.4	6.9	1.35×10^6
		A37_3oxyFCEMFC@9	14.6	0.4	27.7	0.7	0.2	0.4	3.8	6.1	1.89×10^6

Particles	Mineral	Spot #	$\delta^{17}O$	2σ	$\delta^{18}O$	2σ	$\Delta^{17}O$	2σ	$FeCO_3$*	$MnCO_3$*	OH^- intensity (counts/second)
C0009	Dolomite	C009_dolo@3	12.9	0.7	25.4	0.7	–0.3	0.8	2.9	4.7	1.71×10^5
		C009_dolo2@1	15.4	0.8	27.4	0.6	1.1	0.7	4.1	7.7	5.40×10^5
		C009_dolo2@2	14.1	0.9	24.2	0.6	1.4	0.9	5.3	2.3	9.80×10^5
		C009_dolo2@3	13.1	0.8	22.7	0.6	1.2	0.7	4.9	5.7	5.30×10^5

Supplementary Table 1 (continued).

Particles	Mineral	Spot #	$\delta^{17}O$	2σ	$\delta^{18}O$	2σ	$\Delta^{17}O$	2σ	$FeCO_3$*	$MnCO_3$*	OH^- intensity (counts/second)
C0009	Dolomite	C009_dolo2@4	15.2	0.8	27.0	0.5	1.2	0.8	5.3	2.3	6.90×10^5
	Ca-carbonate	C009_ca@1	19.1	1.0	35.1	1.7	0.8	1.0	1.3	n.d.	5.40×10^5
		C009_ca@2	19.4	0.9	37.3	1.6	0.0	0.9	1.3	n.d.	2.00×10^5
		C009_ca@3	22.5	1.0	39.0	1.7	2.2	1.0	1.1	n.d.	3.80×10^5
		C009_ca@5	18.7	1.0	35.0	1.6	0.5	1.0	1.5	n.d	1.13×10^5
		C009_ca@6	18.9	0.9	34.2	1.5	1.1	1.0	1.5	n.d.	1.20×10^5
		C009_ca@7	19.3	0.9	36.4	1.7	0.3	0.9	1.5	n.d	3.75×10^5

* Data from Yamaguchi et al. (2022).
$FeCO_3$ and $MnCO_3$ are mol%.
n.d.: not detected.

Supplementary Table 2. Oxygen-isotope compositions of magnetite in A0037 and C0009.

Particles	Mineral	Spot #	$\delta^{17}O$	2σ	$\delta^{18}O$	2σ	$\Delta^{17}O$	2σ	FeO*	OH$^-$ intensity (counts/second)
A0037	Magnetite	A37_3oxyFCEMFC@10	3.7	0.5	3.0	0.9	2.1	0.4	93.0	6.70×10^6
		A37_3oxyFCEMEM@1	4.8	1.0	1.7	1.0	3.9	0.9	92.8	3.58×10^5
		A37_3oxyFCEMEM@5	3.1	0.8	1.0	0.7	2.6	0.8	93.0	4.00×10^5
		A37_3oxyFCEMEM@10	4.6	1.1	2.8	1.2	3.1	0.9	92.0	2.48×10^5
C0009	Magnetite	C0009_sqr_mgt@1	–2.8	1.0	–11.2	1.3	3.0	0.9	n.a.	2.36×10^5
		C0009_Mgt2@7	5.3	0.9	3.1	0.9	3.7	0.9	93.3	6.60×10^5
		C0009_Mgt2@8	3.0	0.8	2.4	0.7	1.7	0.8	93.4	7.20×10^5
		C0009_Mgt2@9	3.8	0.9	–0.2	0.8	3.9	0.9	n.a.	4.80×10^5
		C0009_Mgt2@10	4.0	0.9	2.5	0.7	2.7	1.0	n.a.	6.80×10^5
		C0009_Mgt2@11	5.3	0.8	4.1	0.7	3.1	0.9	n.a.	5.80×10^5

Data from Yamaguchi et al. (2022).

FeO is wt%.

n.a.: not analyzed.

Supplementary Table 3. Carbon-isotope compositions of carbonates in A0037 and C0009.

Particles	Mineral	Spot #	$\delta^{13}C$	2σ
A0037	Dolomite	A37_C_dolo@1.asc	55.4	1.6
		A37_C_dolo@2.asc	62.3	1.3
		A37_C_dolo@3.asc	58.9	1.6
		A37_C_dolo@5.asc	58.2	1.2
		A37_C_dolo@6.asc	72.1	1.0
		A37_C_dolo@7.asc	70.5	1.1
		A37_C_dolo@8.asc	72.0	1.0
		A37_C_dolo@9.asc	69.7	1.0
		A37_C_dolo@10.asc	57.1	1.2
		A37_C_dolo@11.asc	68.1	1.0
		A37_C_dolo@12.asc	74.4	1.1
		A37_C_dolo@13.asc	71.0	0.9
		A37_C_dolo@14.asc	72.6	1.1
C0009	Dolomite	C0009_C_dolo@1.asc	74.5	1.0
		C0009_C_dolo@2.asc	73.3	0.9
		C0009_C_dolo@3.asc	69.7	0.8
		C0009_C_dolo@4.asc	74.3	0.8
		C0009_C_dolo@5.asc	64.0	0.8
		C0009_C_dolo@6.asc	66.4	1.0
		C0009_C_dolo@7.asc	69.3	1.1
C0009	Ca-carbonate	C0009_C_ca@1.asc	96.9	1.1
		C0009_C_ca@3.asc	72.0	1.3
		C0009_C_ca@4.asc	70.9	1.4

Supplementary Table 4. Mn-Cr isotope data of carbonates in A0037 and C0009.

Particle	Mineral	Spot #	$^{55}Mn/^{52}Cr$	2σ	$^{53}Cr/^{52}Cr$	2σ	$\delta^{53}Cr$	2σ	# cycles	RSF used (2SE)
A0037	Dolomite	A37@1	232	47	0.11646	0.00116	26	10	30	0.8 ± 0.14
		A37@2	23	5	0.11535	0.00108	17	10	30	0.8 ± 0.14
		A37@3	44	14	0.11473	0.00108	11	10	30	0.8 ± 0.14
		A37@4	51	13	0.11557	0.00110	19	10	30	0.8 ± 0.14
		A37@5	122	40	0.11498	0.00114	13	10	14	0.8 ± 0.14
		A37_Feb15@6	601	110	0.11982	0.00134	56	12	26	0.8 ± 0.14
		A37_Feb15@7	7377	1333	0.16786	0.00374	480	33	30	0.8 ± 0.14
		A37_Feb15@8	2787	572	0.13394	0.00224	181	20	30	0.8 ± 0.14
		A37_Feb15@9	283	63	0.11560	0.00118	19	10	30	0.8 ± 0.14
		A37_Feb15@10	1972	371	0.12495	0.00296	101	26	11	0.8 ± 0.14
		A37_Feb15@12	606	239	0.11786	0.00138	39	12	7	0.8 ± 0.14
		A37_Feb15@13	404	129	0.11702	0.00160	31	14	10	0.8 ± 0.14
		A37_Feb15@14	4765	865	0.14324	0.00354	262	31	30	0.8 ± 0.14
		A37_Feb15@15	6209	1247	0.15734	0.00518	387	46	27	0.8 ± 0.14
		A37_Feb15@17	1387	466	0.12365	0.00212	90	19	14	0.8 ± 0.14
		A37_Feb15@18	9404	1801	0.17455	0.00550	538	48	30	0.8 ± 0.14
		A37_Feb15@19	5204	1047	0.15095	0.00302	330	27	15	0.8 ± 0.14
		A37_Feb15@21	5518	1204	0.15457	0.00800	362	71	14	0.8 ± 0.14
		A37_Feb15@23	2368	433	0.13134	0.00178	158	16	30	0.8 ± 0.14
		A37_Feb15@24	6401	1151	0.16061	0.00362	416	32	30	0.8 ± 0.14
C0009	Dolomite	C9@2	1393	332	0.12229	0.00332	78	29	9	0.8 ± 0.14
		C9@3	4044	822	0.13980	0.00286	232	25	9	0.8 ± 0.14
		C9@4	2252	478	0.12912	0.00258	138	23	12	0.8 ± 0.14
		C9@5	2445	942	0.12950	0.00408	141	36	30	0.8 ± 0.14
		C9@6	2833	700	0.13138	0.00278	158	25	30	0.8 ± 0.14
		C9@7	3070	741	0.13189	0.00318	162	28	20	0.8 ± 0.14
		C9@8	2729	479	0.12945	0.00194	141	17	11	0.8 ± 0.14
		C9@9	1121	202	0.11905	0.00420	49	37	30	0.8 ± 0.14

Supplementary Table 4 (continued).

Particle	Mineral	Spot #	$^{55}Mn/^{52}Cr$	2σ	$^{53}Cr/^{52}Cr$	2σ	$\delta^{53}Cr$	2σ	# Cycles	RSF used (2SE)
C0009	Dolomite	C9@11	10529	1874	0.18181	0.00412	602	36	12	0.8 ± 0.14
		C9@12	5055	951	0.14578	0.00302	285	27	30	0.8 ± 0.14
		C9@14	1735	509	0.12537	0.00214	105	19	26	0.8 ± 0.14
		C9@16	1650	761	0.12499	0.00362	102	32	10	0.8 ± 0.14
		C9_3EM@3	2243	1175	0.12873	0.00578	135	51	13	0.8 ± 0.14
C0009	Breunnerite	C9@10	3326	680	0.13239	0.00224	167	20	30	0.86 ± 0.14
C0009	Ca-carbonate	C9_3EM@1	32	14	0.11367	0.00978	2	86	10	1.3 ± 0.4
		C9_3EM@2	8	3	0.11772	0.00546	38	48	10	1.3 ± 0.4

Supplementary Table 5. Chemical and isotopic compositions of reference materials used to constrain instrumental mass fractionation during carbon and oxygen stable isotopic analysis of carbonates. Carbon and oxygen isotopic compositions were determined by phosphoric acid digestion and IRMS of CO_2 at UCLA. Elemental compositions were determined using EPMA analysis.

Material name	Mineral	$\delta^{17}O$ SMOW	$\delta^{18}O$ SMOW	$\delta^{13}C$ VPDB	$CaCO_3$	$MgCO_3$	$FeCO_3$	$MnCO_3$
OPTI calcite	Calcite	5.76	11.10	1.42	99.4	0.5	n.d.	n.d.
MS1317	Dolomite	11.80	22.82	−21.13	51.8	48.1	n.d.	0.1
MS1305	Dolomite	10.99	21.24	−1.10	50.8	48.0	1.1	0.1
MS1317J	Dolomite	11.13	21.51	−1.20	51.1	45.8	2.9	0.2
MS1312	Dolomite	11.63	22.48	0.00	51.1	21.6	21.1	6.2

$CaCO_3$, $MgCO_3$, $FeCO_3$, and $MnCO_3$ are mol%.

n.d.: not detected.

Supplementary Table 6. RSF values obtained using depth profiling of ion-implanted materials, where n represents the number of repeat depth profiles. The Mn concentration in each mineral is derived from EPMA data and reported as µg Mn/g.

Mineral	FeCO3 mol%	weighted mean RSF	2SE	n	Mn concentration (ppm)
Calcite	n.d.	1.3	0.84	2	100
Dolomite					
MS1317 (D)	n.d.	0.94	0.18	6	411
MS1305 (D)	0.85	0.76	0.34	2	558
MS1317J (D)	1.4	0.85	0.14	2	1011
MS1318 (D)	8.0	0.72	0.08	5	6244
Magnesite					
MS1223D	0.2	0.96	0.14	2	761
M1952	18.8	0.81	0.10	2	6402
M2035	39.5	0.69	0.21	1	2969
San Carlos Olivine	–	1.03	0.17	2	1029

n.d.: not detected.

Supplementary Table 7. Values used to calculate the RSF from individual depth profiles of carbonate, glass, and San Carlos olivine. A_{52Cr+}_R refers to the total number of counts of implanted $^{52}Cr^+$ detected before using the SRIM simulation to correct for surface contamination (see supplemental text above). A_{52Cr+}_C refers to the total number of counts of $^{52}Cr^+$ detected after surface contamination correction, and is the value used to calculate the RSF. ΔA_{52Cr} represents the fractional difference between A_{52Cr+}_C and A_{52Cr+}_R, and is defined as

$$\Delta A_{52Cr+} = \frac{(A_{52Cr+}\_R - A_{52Cr+}\_C)}{A_{52Cr+}\_R}$$

The position and shape of the gaussian derived from SRIM modeling and used to correct for surface contamination are reported as Mean of Gaussian and 1SD.

Name	RSF	2SD	A_{52Cr+}_R (counts)	A_{52Cr+}_C (counts)	ΔA_{52Cr+}	I_{55Mn} (cps)	2SD	D (μm)	t (s)	Gaussian mean (nm)	1SD
Calcite@16	1.32	1.20	152159	102185	0.33	100	10	0.4649	2331	72	37
Calcite@17	1.33	1.20	154536	100183	0.35	97	12	0.4176	2089	72	37
Dolomite											
MS1305@21	0.68	0.38	172564	126476	0.27	1303	44	0.6017	3257	85	33
MS1305@22	0.95	0.52	168933	127681	0.24	916	32	0.4101	2284	85	33
MS1317j@14	0.74	0.10	175584	130843	0.25	2261	56	0.3448	1837	76	33
MS1317j@15	0.95	0.26	168575	127908	0.24	1825	58	0.5383	2730	80	33
MS1317@19	0.75	0.32	165357	128631	0.22	895	38	0.4992	2608	88	32
MS1317@20	1.72	0.71	148793	120931	0.19	372	20	0.5167	2679	88	32
MS1317_@23	0.78	0.32	153109	121795	0.20	858	36	0.9917	4963	92	32
MS1317_@24	1.56	0.66	150681	120610	0.20	426	30	0.9972	4961	95	32
MS1317_@25	1.02	0.42	150376	122448	0.19	673	34	1.015	4962	96	32
MS1317_@26	0.74	0.30	156392	127232	0.19	940	34	0.9951	4962	93	32
MS1318_fa2500_max80@43	0.70	0.16	404863	288031	0.29	30411	546	0.3228	1895	78	33
MS1318@12	0.74	0.18	199599	139926	0.30	14920	194	0.6268	3451	75	33
MS1318@13	0.73	0.18	191658	134540	0.30	14761	200	0.5582	3003	78	33
MS1318_@28	0.74	0.18	186121	132740	0.29	13642	244	0.4727	2678	80	33
MS1318_@29	0.70	0.18	187791	127794	0.32	13961	338	0.5067	2579	80	33

Supplementary Table 7 (continued).

Name	RSF	2SD	A_{52Cr+}_R (counts)	A_{52Cr+}_C (counts)	ΔA_{52Cr+}	I_{55Mn} (cps)	2SD	D (μm)	t (s)	Gaussian mean (nm)	1SD
Magnesite											
MAGN_M2035@42	0.69	0.22	766726	769886	0.00	46956	1020	0.7215	3600	99	38
MAGN_MS1223D@33	0.88	0.18	443427	438043	0.01	5601	162	0.6594	3173	96	36
MAGN_MS1223D@34	1.09	0.22	450860	448074	0.01	4279	110	0.5084	2632	94	36
MAGN_MS1952@35	0.80	0.12	469061	466691	0.01	53761	3594	0.4671	2386	94	36
MAGN_MS1952@36	0.82	0.14	426366	423043	0.01	48211	3873	0.5067	2579	91	36
NIST Glass											
MAGN_NIST612@32	1.04	0.14	2089105	2075818	0.01	617	52	0.667	4962	115	40
MAGN_NIST614@30	1.06	0.32	2052221	2047233	0.00	23	8	0.661	4668	120	40
San Carlos Olivine											
SCOL@10	1.02	0.22	1474422	1455160	0.01	9837	1910	0.3971	4713	90	38
SCOL@11	1.05	0.28	1347762	1324634	0.02	9059	2274	0.3922	4485	95	38

References

1. McCain, K. A., Liu, M.-C. & McKeegan, K. D. Calibration of matrix-dependent biases in isotope and trace element analyses of carbonate minerals. *Journal of Vacuum Science & Technology B* **38**, 044005 (2020).

2. Ziegler, J. F., Ziegler, M. D. & Biersack, J. P. SRIM - The stopping and range of ions in matter (2010). *NIMPB* **268**, 1818–1823 (2010).

3. Doyle, P. M., Jogo, K., Nagashima, K., Huss, G. R. & Krot, A. N. Mn–Cr relative sensitivity factor in ferromagnesian olivines defined for SIMS measurements with a Cameca ims-1280 ion microprobe: Implications for dating secondary fayalite. *Geochimica et Cosmochimica Acta* **174**, 102–121 (2016).

4. Virtanen, P. *et al.* SciPy 1.0: fundamental algorithms for scientific computing in Python. *Nature Methods* **17**, 261–272 (2020).

5. York, D., Evensen, N. M., Martínez, M. L. & De Basabe Delgado, J. Unified equations for the slope, intercept, and standard errors of the best straight line. *American Journal of Physics* **72**, 367–375 (2004).

6. Huberty, J. M. *et al.* Crystal orientation effects in $\delta^{18}O$ for magnetite and hematite by SIMS. *Chemical Geology* **276**, 269–283 (2010).

7. Hayles, J., Gao, C., Cao, X., Liu, Y. & Bao, H. Theoretical calibration of the triple oxygen isotope thermometer. *Geochimica et Cosmochimica Acta* **235**, 237–245 (2018).

8. Zheng, Y.-F. Oxygen isotope fractionation in magnetites: structural effect and oxygen inheritance. *Chemical Geology* **121**, 309–316 (1995).

9. Telus, M., Alexander, C. M. O., Hauri, E. H. & Wang, J. Calcite and dolomite formation in the CM parent body: Insight from in situ C and O isotope analyses. *Geochimica et Cosmochimica Acta* **260**, 275–291 (2019).

10. Kim, S.-T. & O'Neil, J. R. Equilibrium and nonequilibrium oxygen isotope effects in synthetic carbonates. *Geochimica et Cosmochimica Acta* **61**, 3461–3475 (1997).

11. Cole, D. R. *et al.* An experimental and theoretical determination of oxygen isotope fractionation in the system magnetite-H2O from 300 to 800°C 1 1Associate editor: E. M. Ripley. *Geochimica et Cosmochimica Acta* **68**, 3569–3585 (2004).

12. Horita, J. Oxygen and carbon isotope fractionation in the system dolomite–water–CO_2 to elevated temperatures. *Geochimica et Cosmochimica Acta* **129**, 111–124 (2014).

13. Saccocia, P. J., Seewald, J. S. & Shanks, W. C. Oxygen isotope fractionation in the portlandite–water and brucite–water systems from 125 to 450°C, 50MPa. *Geochimica et Cosmochimica Acta* **169**, 137–151 (2015).